Article

CLSTN3B promotes lipid droplet maturation and lipid storage in mouse adipocytes

Check for updates

Chuanhai Zhang[1], Mengchen Ye[2], Kamran Melikov[3], Dengbao Yang[1], Goncalo Dias do Vale[4], Jeffrey McDonald[4], Kaitlyn Eckert[4], Mei-Jung Lin[1] & Xing Zeng[1]

Interorganelle contacts facilitate material exchanges and sustain the structural and functional integrity of organelles. Lipid droplets (LDs) of adipocytes are responsible for energy storage and mobilization responding to body needs. LD biogenesis defects compromise the lipid-storing capacity of adipocytes, resulting in ectopic lipid deposition and metabolic disorders, yet how the uniquely large LDs in adipocytes attain structural and functional maturation is incompletely understood. Here we show that the mammalian adipocyte-specific protein CLSTN3B is crucial for adipocyte LD maturation. CLSTN3B employs an arginine-rich segment to promote extensive contact and hemifusion-like structure formation between the endoplasmic reticulum (ER) and LD, allowing ER-to-LD phospholipid diffusion during LD expansion. CLSTN3B ablation results in reduced LD surface phospholipid density, increased turnover of LD-surface proteins, and impaired LD functions. Our results establish the central role of CLSTN3B in the adipocyte-specific LD maturation pathway that enhances lipid storage and maintenance of metabolic health under caloric overload in mice of both sexes.

Adipocytes store excess energy in the form of neutral lipids, primarily triacylglycerides (TG). Insufficient lipid-storing capacity of adipocytes results in ectopic lipid deposition in extra-adipose organs and drives the pathogenesis of metabolic disorders, such as type II diabetes[1]. Enhancing lipid storage in adipocytes with peroxisome proliferator activated receptor gamma (PPARG) agonists improves insulin sensitivity[2,3]. However, the clinical use of PPARG agonists has been hampered by cardiovascular side effects[4], calling for the elucidation of additional limiting factors governing the lipid-storing capacity of adipocytes.

Cells store neutral lipids in lipid droplets (LDs), organelles coated with a monolayer of phospholipids and various LD-targeting proteins. LD surface structures protect the internal lipid storage from unregulated lipolysis while sensitizing lipid mobilization to hormonal stimulation[5,6]. LD biogenesis occurs at the endoplasmic reticulum (ER), facilitated by an ER integral membrane protein known as SEIPIN.

Structural studies revealed that a ring of SEIPIN monomers forms a cage-like structure likely promoting TG phase separation within the ER membrane leaflets and subsequent budding into nascent LDs[7–9]. Nascent LDs continue to acquire surface phospholipids and proteins during their maturation process. Growing LDs promote the targeting and activation of CTP:Phosphocholine Cytidyltransferase (CCT), an enzyme in the phosphatidylcholine (PC) synthetic pathway, to the LD surface, driving increased PC synthesis to meet the demand of expanding LD surface[10]. Nevertheless, the final step of phospholipid synthesis occurs at the ER membrane and how those phospholipids are delivered to the LD surface remains largely unclear. Proteins are targeted to LDs via two distinct pathways (Class I and Class II)[6,11,12]. Class I proteins have long hydrophobic stretches and translocate from the ER to LD via membrane continuities. Class II proteins are recruited from cytosol to the LD surface by their amphipathic helices (AH). Impaired LD biogenesis compromises the lipid-storage capacity of adipocytes

[1]Department of Physiology, UT Southwestern Medical Center, Dallas, TX, USA. [2]Department of Molecular and Cell Biology, University of California Berkeley, Berkeley, CA, USA. [3]Section on Membrane Biology, Eunice Kennedy Shriver National Institute of Child Health and Human Development, National Institutes of Health, Bethesda, MD, USA. [4]Center for Human Nutrition, UT Southwestern Medical Center, Dallas, TX, USA. ✉e-mail: xing.zeng@utsouthwestern.edu

and increases susceptibility to metabolic diseases[13–15]. How adipocytes employ cell type-specific mechanisms to attain structural and functional maturation of their uniquely large and dynamic LDs remains to be fully understood.

The ER makes extensive contact with other organelles and plays a crucial role in the maturation and homeostasis of other organelles[16]. Recent studies have elucidated many proteins contributing to the formation of ER/LD contacts that mediate the exchange of proteins or lipids between the two organelles[17–25]. Nevertheless, the detailed mechanism by which such material transfers take place, especially in the cellular context of adipocytes, has remained largely obscure.

We previously cloned an unannotated gene specifically expressed in mammalian adipocytes that we named Calsyntenin 3β (CLSTN3B)[26]. We showed that ablation of CLSTN3B leads to defective sympathetic innervation of the brown adipose tissue (BAT) and impaired thermogenesis through downregulating a neurotrophic protein S100B. Another study showed a distinct function of CLSTN3B to enforce the multilocular morphology of brown adipocytes by restricting CIDEA-mediated LD fusion[27]. Interestingly, CLSTN3B is also expressed at a significant level in monolocular white adipocytes with minimal sympathetic innervation and thermogenic activity, suggesting that a gap still exists in our understanding of CLSTN3B function.

Here, we show that CLSTN3B works at the ER/LD interface to promote adipocyte LD maturation. We found that CLSTN3B facilitates ER-to-LD phospholipid diffusion during LD expansion. This is achieved by a unique arginine-rich segment of CLSTN3B that induces the formation of hemifusion-like structures between the ER cytosolic leaflet and the LD monolayer. CLSTN3B deficiency results in structurally and functionally impaired LDs characterized by reduced surface phospholipid density and increased turnover of LD-targeting proteins. Consequently, ablating CLSTN3B from white adipocytes results in reduced lipid storage in the perigonadal white adipose tissue (pgWAT) and increases susceptibility to ectopic lipid deposition and onset of metabolic disorders at the animal level, whereas enhancing CLSTN3B expression in white adipocytes yields the opposite phenotype. Our results demonstrate how CLSTN3B-mediated inter-organelle communication promotes LD maturation, enhances lipid storage in adipocytes, and translates into physiological significance at the animal level.

Results

CLSTN3B enhances lipid storage in perigonadal white adipocytes

We previously showed that CLSTN3B is highly expressed in brown adipocytes and contributes to thermogenesis[26]. To probe the physiological relevance of CLSTN3B to white adipocytes primarily responsible for TG storage but not thermogenesis, we employed a condition favoring TG deposition: high-fat diet (HFD) feeding at thermoneutrality (28–30 C). Under this condition, clstn3b^{-/-} male mice had significantly reduced pgWAT masses, smaller adipocyte sizes in the pgWAT, more severe liver steatosis, higher serum free fatty acid (FFA) levels, and concomitant glucose intolerance compared with WT mice (Fig. 1a–g). Similar phenotypes were observed in female mice at thermoneutrality or male mice at room temperature (Supplementary Fig. 1a–g), and likely reflect an inability of the pgWAT to expand upon HFD feeding instead of defective adipogenesis or lipodystrophy, because age-matched clstn3b^{-/-} male mice maintained on chow diet have larger WAT masses and higher expression levels of PPARG targets or de novo lipogenesis (DNL)-related genes than the WT (Supplementary Fig. 1h–l). Importantly, signs of impaired WAT lipid storage, including elevated serum FFA and liver TG levels were still observed in clstn3b^{-/-} mice on chow diet (Supplementary Fig. 1m, n). These results suggest that the ablation of CLSTN3B impairs lipid storage in the pgWAT and promotes ectopic lipid deposition, especially under the HFD condition. The reduced pgWAT mass is unlikely caused by defective sympathetic innervation as previously noted in the BAT of

the clstn3b^{-/-} mice[26], because innervation deficiency is expected to cause increased lipid accumulation, contrary to the reduced pgWAT masses as observed. Furthermore, pgWAT receives minimal parenchymal sympathetic innervation[28], which is not affected by CLSTN3B ablation (Supplementary Fig. 2).

We then examined whether the pgWAT phenotype resulted from CLSTN3B deficiency in brown or white adipocytes. We first restored CLSTN3B expression specifically in brown adipocytes of the clstn3b^{-/-} mice with a previously published adenovirus-associated virus (AAV) approach[26]. Although AAV-delivered CLSTN3B transgene achieved a ~70-fold overexpression of CLSTN3B in the BAT compared with WT mice and completely reversed the BAT defects, it failed to improve pgWAT lipid storage and ectopic lipid deposition (Fig. 2a–c and Supplementary Fig. 3a), indicating that CLSTN3B deficiency in white adipocytes is primarily responsible for the phenotype. As an alternative approach to delineate the contribution from brown and white adipocyte-derived CLSTN3B to the metabolic phenotypes, we constructed pan-adipocyte CLSTN3B and brown adipocyte-specific CLSTN3B knockout (KO) mice (adq-cre, clstn3b^{fl/fl}; ucp1-cre, clstn3b^{fl/fl}) and subjected them to HFD feeding at thermoneutrality. Whereas the pan-adipocyte CLSTN3B KO mice displayed similar metabolic defects to the global clstn3b^{-/-} mice, the brown adipocyte-specific KO mice were indistinguishable from their WT control littermates (Fig. 2d–i). These data again support that CLSTN3B expression in white adipocytes is responsible for enhancing lipid storage in the pgWAT.

To complement the loss-of-function models, we analyzed transgenic mice overexpressing CLSTN3B in all adipocytes (ATg, adq-cre, clstn3b[tg/o]) or only brown adipocytes (UTg, ucp1-cre, clstn3b[tg/o]) fed with HFD. Only the ATg but not the UTg mice displayed improved pgWAT lipid storage and ameliorated liver steatosis compared with littermate control mice housed at thermoneutrality or RT (Fig. 3a–l and Supplementary Fig. 3b–e), again highlighting the requirement of CLSTN3B expression in white adipocytes for improving lipid storage in the pgWAT and metabolic health.

CLSTN3B enhances LD phospholipid and protein levels

We then performed lipolytic assays with isolated clstn3b^{-/-} white adipocytes to examine the reason underlying reduced lipid-storage capacity and found that those cells exhibited higher basal lipolysis rates and blunted responses to norepinephrine (NE) stimulation with similar levels of Hormone Sensitive Lipase (HSL) phosphorylation to WT cells (Fig. 4a and Supplementary Fig. 4a). These data suggest that clstn3b^{-/-} white adipocytes have impaired LD functionality. Clstn3b^{-/-} brown adipocytes displayed a similar phenotype (Fig. 4b), indicating that CLSTN3B may enhance LD functionality in all adipocytes.

To understand the molecular basis of the abnormal lipolytic behavior of clstn3b^{-/-} adipocytes, we conducted a systematic analysis of the LD surface structure. We first developed a method to measure LD surface phospholipid density (Supplementary Fig. 4b–d) and found that the area per phospholipid molecule is 71.7 ± 3.5 Å^2 on WT brown adipocyte LD and 88.3 ± 4.6 Å^2 on KO brown adipocyte LD (Fig. 4c). Similarly, the area per phospholipid molecule on WT white adipocyte LD is 79.8 ± 4.1 Å^2 and 99.8 ± 4.2 Å^2 on KO white adipocyte LD (Fig. 4c). Phospholipidomics analysis showed a uniform decrease across a wide range of phospholipid species (Supplementary Fig. 4e). Taken together, these results show CLSTN3B ablation causes reduced phospholipid densities on adipocyte LDs.

We next performed proteomics analyses of adipocyte LDs isolated from WT and clstn3b^{-/-} mice (Supplementary Data file). Significantly downregulated proteins in the clstn3b^{-/-} brown or white adipocyte LD samples relative to the WT (Fig. 4d, e and Supplementary Fig. 4f, g) included the following groups: 1) AH-containing LD-targeting proteins, including perilipins and CIDE-proteins, and their binding partners, including ABHD5 (CGI-58) and PNPLA2 (ATGL); 2) Proteins involved in membrane fusion: including multiple RABs and the
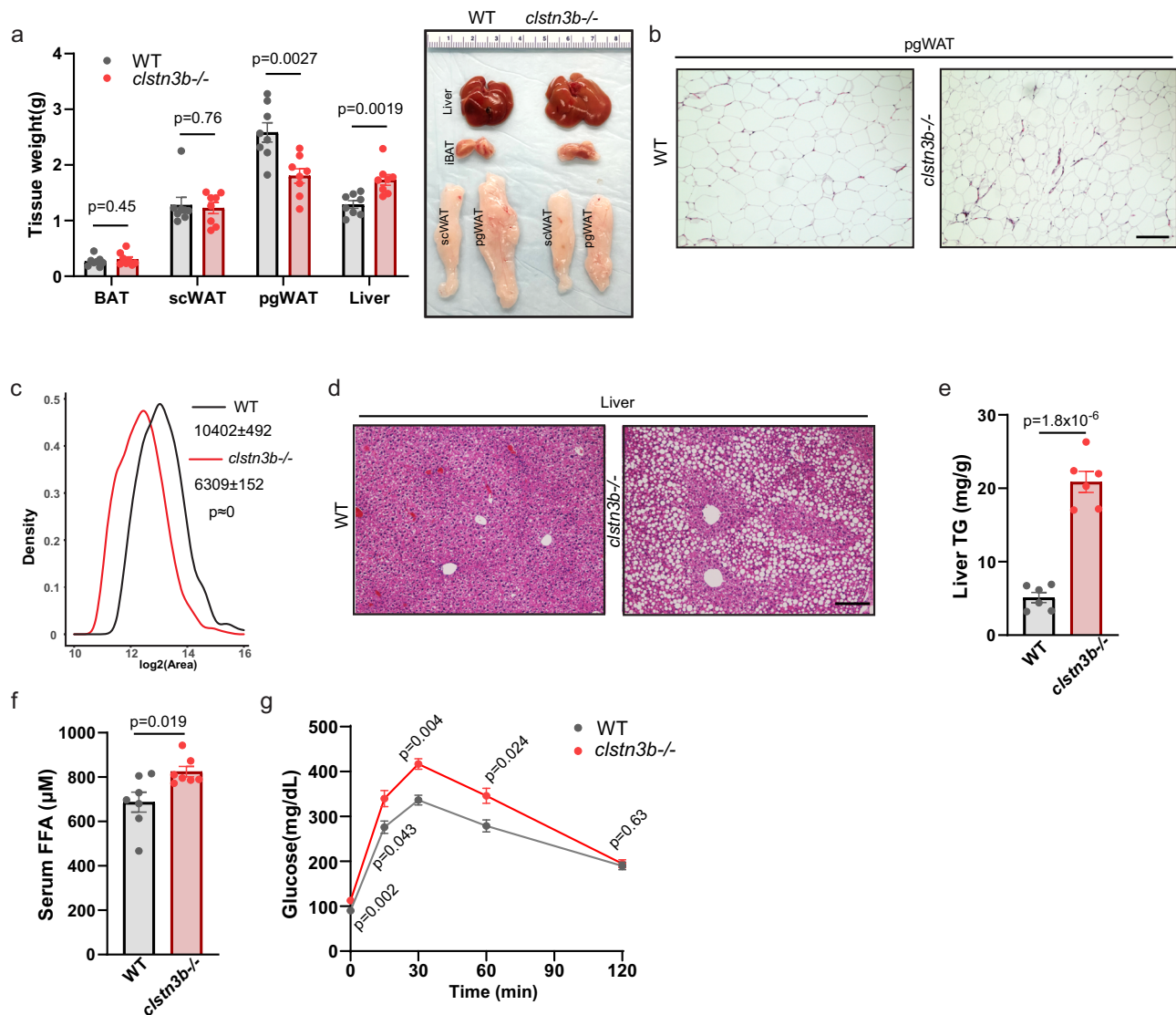
Fig. 1 | CLSTN3B deficiency impairs lipid storage in the perigonadal white adipose tissue. Tissue weights ($n = 8$) and gross appearances (**a**), pgWAT histology (**b**), pgWAT adipocyte size distributions (**c**), liver histology (**d**), liver TG contents ($n = 6$) (**e**), serum FFA ($n = 7$) (**f**), and glucose tolerance test ($n = 7$) (**g**) of WT and $clstn3b^{-/-}$ mice on HFD at thermoneutrality. Scale bar: 100 µm. Data are mean ± s.e.m. Statistical significance was calculated by unpaired Student's two-sided t test for (**a**, **c**, **e**, **f**), and Two-way Repeated Measurement ANOVA for (**g**). Source data are provided as a Source Data file.

Transport Protein Particle Complex subunits (TRAPC). The down-regulation of PLIN1 was verified by Western blot (Supplementary Fig. 4h) and may be particularly relevant to the abnormal lipolytic behavior of $clstn3b^{-/-}$ adipocytes and the metabolic phenotype of $clstn3b^{-/-}$ mice, because $plin1^{-/-}$ adipocytes and mice phenocopy their $clstn3b^{-/-}$[29,30] counterparts. The mRNA levels of downregulated LD proteins were not significantly different between WT and $clstn3b^{-/-}$ brown or white adipocytes (Supplementary Fig. 4i). Taken together, our results suggest that LDs in $clstn3b^{-/-}$ adipocytes are poorly covered by phospholipids and LD-targeting proteins, which may cause increased accessibility of the TG core to lipases and thus explain the elevated level of basal lipolysis. Meanwhile, the reduced recruitment of CGI-58 may limit ATGL activation upon adrenergic receptor activation and thus explain the blunted response to NE stimulation.

The simultaneous downregulation of phospholipids and AH-containing proteins raises a conundrum because LDs with decreased phospholipid packing are expected to recruit more AH-containing proteins[31]. Previous studies demonstrated cooperative binding of AHs and phospholipids at the oil-water interface[32,33]. We therefore hypothesized that LD surface phospholipids may promote better retaining

and reduced turnover of AH-containing proteins. This idea is supported by a higher turnover rate of LD-bound PLIN1-mCherry in $clstn3b^{-/-}$ brown adipocyte (Fig. 4f, g), a stronger propensity for a PLIN1 AH peptide to dissociate from neat triolein droplets than phospholipid-coated triolein droplets (Fig. 4h, i), and a shorter half-life of PLIN1 in $clstn3b^{-/-}$ brown adipocytes (Fig. 4j, k). Taken together, our results suggested that CLSTN3B may reduce AH-containing protein turnover by ensuring optimal phospholipid/protein packing on the LD surface.

The arginine-rich region of CLSTN3B promotes extensive ER/LD contact

We then investigated the mechanism underlying CLSTN3B's ability to enhance LD structure and function and promote white adipocyte lipid storage. A previous study identified that CLSTN3B localizes to ER/LD contact site by an N-terminal LD-localization domain and a C-terminal ER-transmembrane domain[27], which was independently discovered by us (Supplementary Fig. 5a–h). This study also proposed that CLSTN3B inhibits CIDE protein-mediated LD fusion[27]. However, this mechanism can hardly account for CLSTN3B's effect on white adipocyte lipid
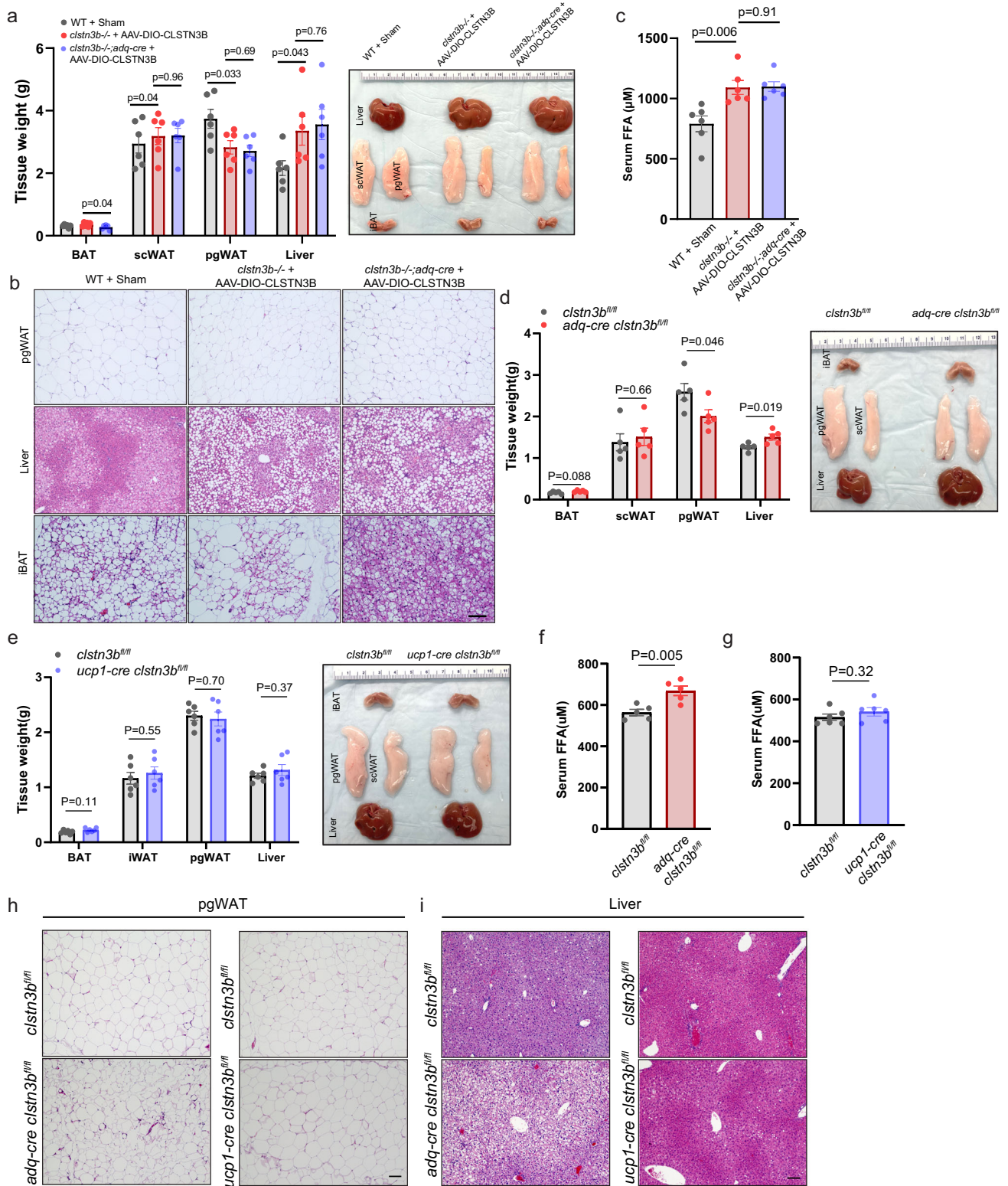
Fig. 2 | White but not brown adipocyte-derived CLSTN3B promotes lipid storage in the perigonadal white adipose tissue and suppresses ectopic lipid deposition. Tissue weights and gross appearances (**a**), pgWAT, liver and BAT histology (**b**), and serum FFA (**c**) of WT mice with sham surgery, *clstn3b*^{−/−}, or *clstn3b*^{−/−}; *adq-cre* mice receiving AAV-DIO-*clstn3b* injection into the iBAT maintained on HFD at thermoneutrality (*n* = 6). Tissue weights and gross appearances of pgWAT and liver (**d**, **e**), serum FFA (**f**, **g**), pgWAT and liver histology (**h**, **i**) of *adq-cre clstn3b*^{fl/fl} (*n* = 5), *ucp1-cre clstn3b*^{fl/fl} (*n* = 6) mice and *cre*-negative littermates on HFD at thermoneutrality. Scale bar: 100 μm. Data are mean ± s.e.m. Statistical significance was calculated by one-way ANOVA with Tukey's post hoc test for (**a**), and unpaired Student's two-sided *t* test for (**c**–**g**). Source data are provided as a Source Data file.
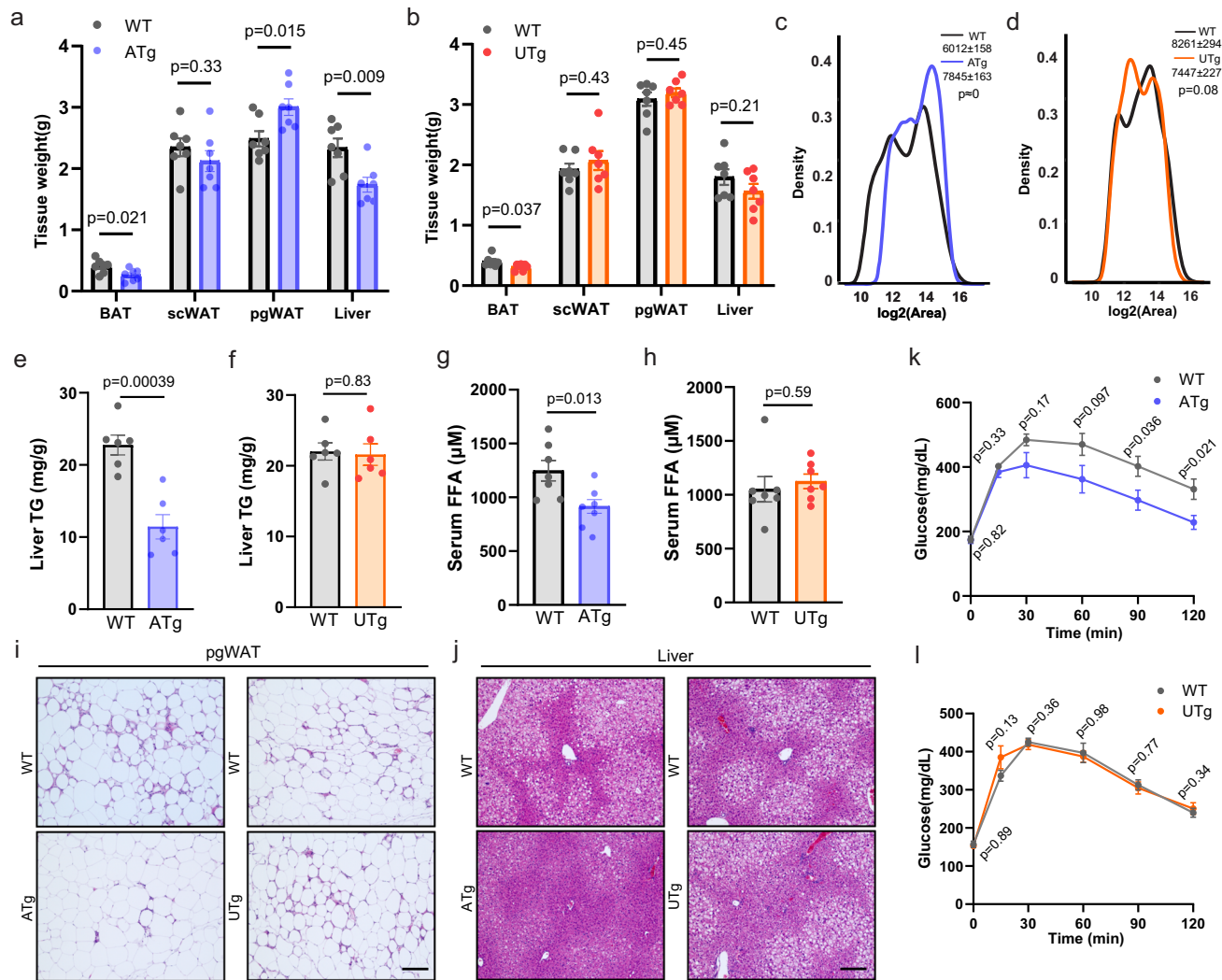
Fig. 3 | Transgenic overexpression CLSTN3B in white adipocyte enhances lipid storage in perigonadal white adipose tissue. Tissue weights ($n = 7$) (**a**, **b**), pgWAT adipocyte size distributions (**c**, **d**), liver TG contents ($n = 6$) (**e**, **f**), serum FFA ($n = 7$) (**g**, **h**), pgWAT and liver histology (**i**, **j**), and glucose tolerance test (**k**, **l**) of *adq-cre clstn3b* transgenic mice ($n = 7$), *ucp1-cre clstn3b* transgenic mice ($n = 7$) and WT littermates on HFD at thermoneutrality. Scale bar: 100 μm. Data are mean ± s.e.m. Statistical significance was calculated by unpaired Student's two-sided *t* test for (**a**, **b**, **e**–**h**), two-sided Wilcoxon text test for (**c**, **d**), and Two-way Repeated Measurement ANOVA for (**k**, **l**). Source data are provided as a Source Data file.

storage for two reasons. First, both WT and *clstn3b*^{-/-} white adipocytes are invariably monolocular (Fig. 1b), indicating that regulation of LD fusion is irrelevant in the context of white adipocytes. Second, WAT lipid storage is impaired by *cidec* ablation or *cidec/cidea* double ablation but enhanced by *cidea* or *cidec* transgenic overexpression[34–36], contradicting the proposed CLSTN3B antagonism on CIDE protein activity. Thus, an uncharacterized mechanism needs to be established to explain CLSTN3B's ability to enhance lipid storage in white adipocytes.

Since the ER is the main source of phospholipids for other organelles[37,38], we hypothesize that CLSTN3B may facilitate ER-to-LD phospholipid transfer during LD growth, explaining why CLTN3B deficiency causes insufficient phospholipid packing on LDs and impaired LD expansion. Phospholipid-binding proteins, such as the VPS13 family members, can promote phospholipid transfer between organelles[39]. Nevertheless, the direct involvement of phospholipid-binding proteins is unlikely for CLSTN3B-mediated ER-to-LD phospholipid transfer because the ER/LD contact induced by CLSTN3B is exceptionally tight that it excludes multiple known LD-targeting proteins, including VPS13C, CIDEA, PLIN1, and PLIN3 (Supplementary Fig. 6a–f). Upon close inspection of CLSTN3B sequence, we noticed

that arginine and proline are the two most frequently appearing residues in the region between the N-terminal LD-targeting domain and the C-terminal transmembrane domain (171–243, arginine 29%, proline 13%) (Fig. 5a). Chi-square test indicates that these two residues are significantly over-represented in this region compared with the mouse proteome ($p < 0.0001$ for R and $p = 0.029$ for P), suggesting they may play important roles in this segment occupying the space between the LD and ER membrane. Arginine-rich peptides interact strongly with membranes through bi-dentate hydrogen bonding with phospholipids[40–44] (Fig. 5b), and are able to promote membrane fusion and phospholipid mixing[41–44]. We therefore hypothesize that CLSTN3B may employ the arginine-rich segment located between the ER and LD membrane to induce fusion between the ER cytosolic leaflet and the LD monolayer and facilitate ER-to-LD phospholipid diffusion during LD growth.

To systematically test this hypothesis, we generated a CLSTN3B RK mutant by replacing 10 arginine residues with lysine (R222, 224, 227, 230, 231, 232, 236, 238, 242, 243 K) to selectively compromise the protein's hydrogen bonding capacity with phospholipids without altering its overall charge. Compared with WT CLSTN3B, the RK mutant exhibited a significantly reduced extent of ER/LD contact
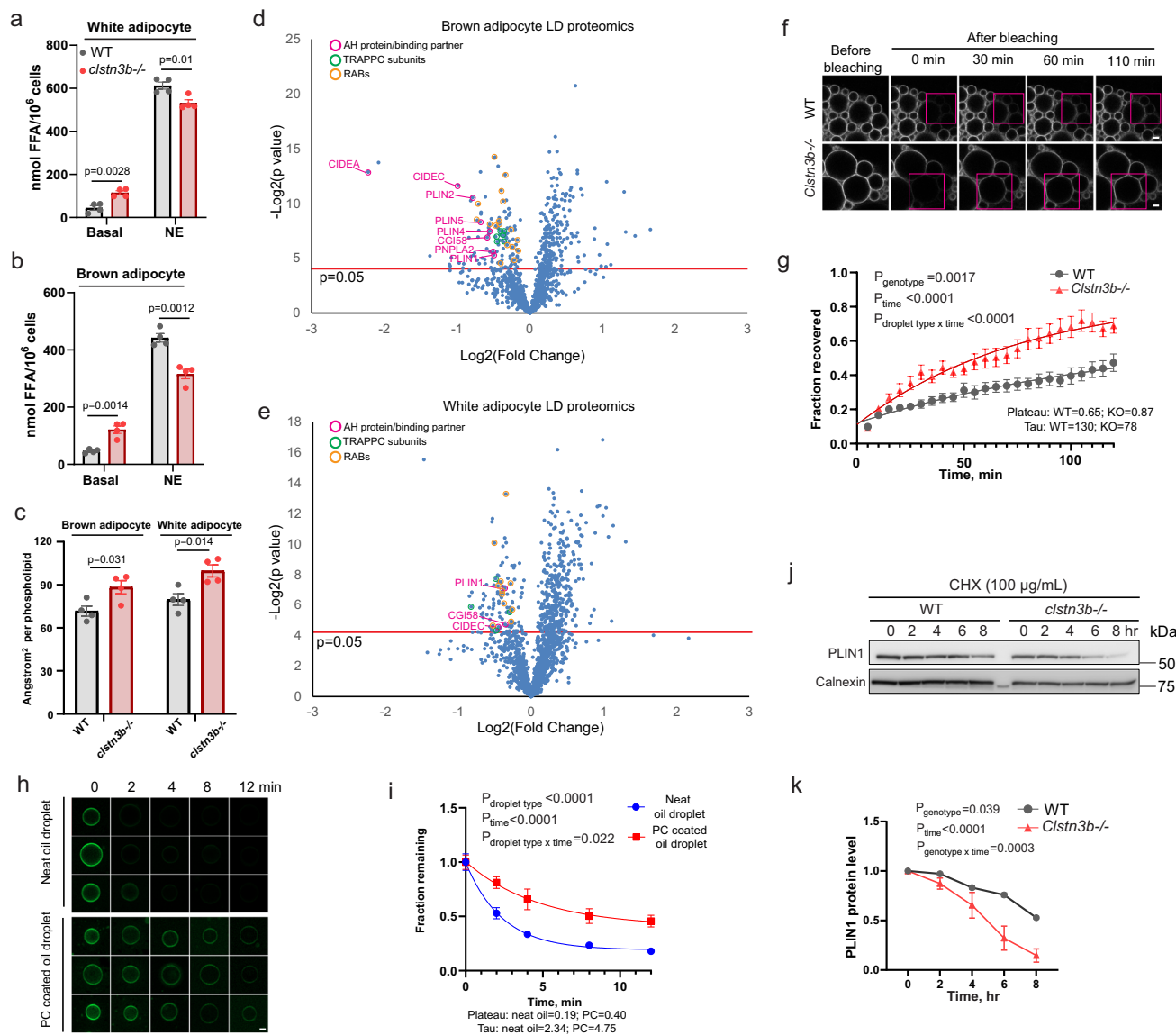
Fig. 4 | CLSTN3B enhances LD phospholipid and protein levels. Lipolysis assay of WT and *clstn3b⁻/⁻* white (**a**) and brown (**b**) adipocytes (*n* = 4 biological replicates). **c** Quantitation of area per phospholipid molecule on brown and white adipocyte LD isolated from WT and *clstn3b⁻/⁻* mice (*n* = 4). Proteomics analysis of brown (**d**) and white (**e**) adipocyte LDs isolated from WT and *clstn3b⁻/⁻* mice (*n* = 4). Representative FRAP images (**f**) and quantitative analysis (*n* = 10 LDs) (**g**) of PLIN1-mcherry turnover rate in WT and *clstn3b⁻/⁻* brown adipocytes. Representative images (**h**) and quantitative analysis (**i**) of fluorescent PLIN1 peptide coating of neat or PC-coated triolein droplets in the presence of excess unlabeled PLIN1 peptide (*n* = 8–18 LDs for each condition). Representative Western blot (**j**) and quantitative analysis (**k**) of PLIN1 half-life by cycloheximide chase in WT and *clstn3b⁻/⁻* brown adipocytes (*n* = 3 biological replicates). Scale bar: 1 μm in (**f**, **h**). Data are mean ± s.e.m. Statistical significance was calculated by unpaired Student's two-sided *t* test for (**a**–**e**), and Two-way Repeated Measurement ANOVA for (**g**, **i**, **k**). No adjustment was made for multiple comparisons for (**d**, **e**). Source data are provided as a Source Data file.

formation as detected by both fluorescence and electron microscopy (Fig. 5c–f). These results thus support a critical role of the arginine-rich segment in inducing extensive close contact between the LD and ER membrane.

The arginine-rich region of CLSTN3B facilitates ER-to-LD phospholipid diffusion

We then investigated the effect of the arginine-rich segment on LD surface phospholipid abundance. LDs from HEK293 cells expressing CLSTN3B displayed 54% higher density of PC and 33% higher density of PE than non-expressing cells, whereas the RK mutant displayed a strongly diminished effect (Fig. 6a). Expressing the N-terminal or the C-terminal fragment of CLSTN3B individually does not alter LD surface phospholipid density (Supplementary Fig. 7a), again supporting that the formation of ER/LD contact is required for this effect.

To obtain direct evidence for CLSTN3B-mediated ER-to-LD phospholipid flow, we employed fixed cell imaging combined with click chemistry labeling of newly synthesized PC. We first induced LD formation in HEK293 cells, labeled newly synthesized PC with alkyne choline for 6 hrs, and then used an azide-fluorophore to visualize labeled PC (Fig. 6b). We compared the fluorescence level on the part of LD surface free from CLSTN3B versus the part in association with CLSTN3B, as this ratio reflects the extent by which newly synthesized PC molecules have translocated from the ER to LD. The results showed in cells expressing WT CLSTN3B, the ratio between labeled PC on the CLSTN3B-free LD surface to the part associated with CLSTN3B is significantly higher than in cells expressing the RK mutant (Fig. 6c, d), suggesting a larger extent of ER-to-LD phospholipid flow mediated by WT CLSTN3B. To avoid interference from ER phospholipids and exclusively focus on LD monolayer phospholipids, we took an
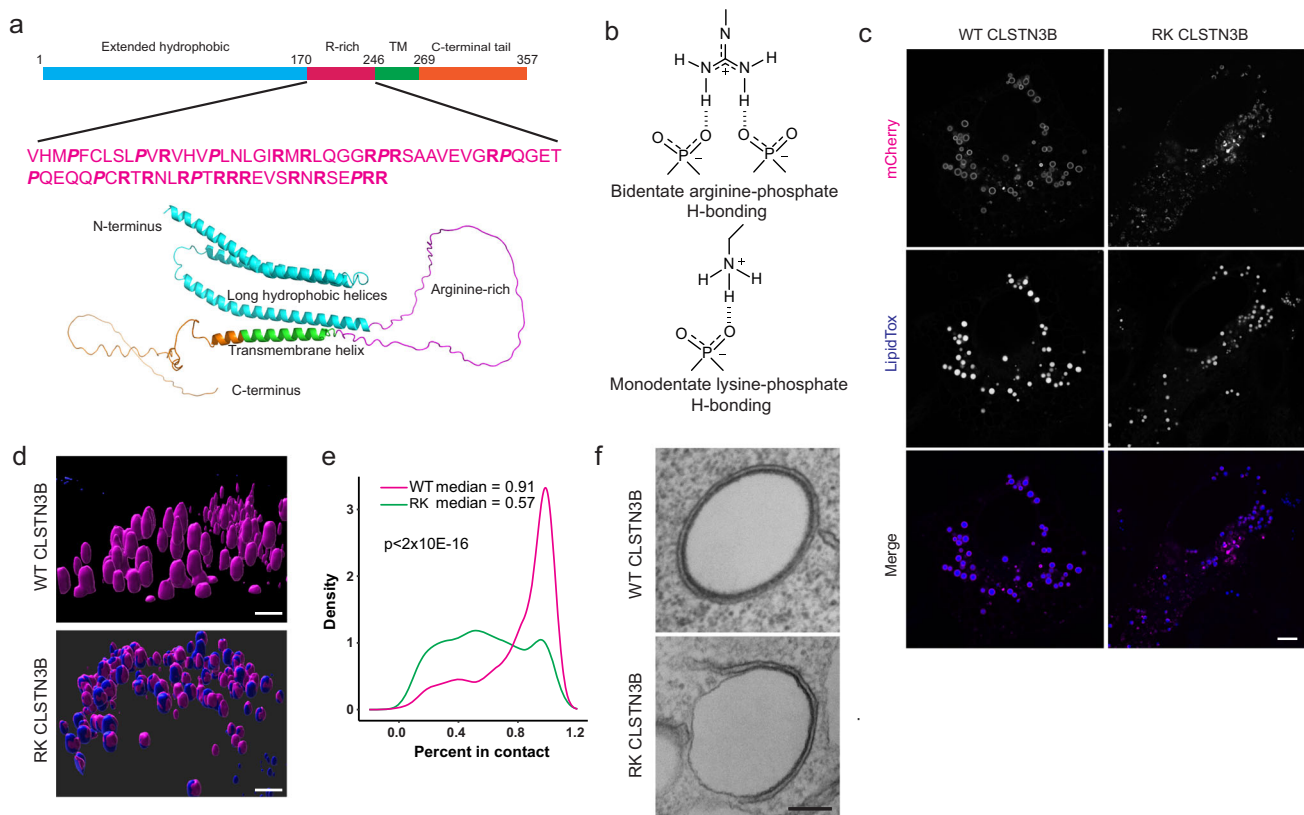
Fig. 5 | The arginine-rich region of CLSTN3B promotes extensive ER/LD contact. **a** Ribbon diagram of AlphaFold predicted structure of CLSTN3B and the distribution of arginine (bold) and proline residues (bold italic) in the arginine-rich region of CLSTN3B (170–246). **b** Illustration of arginine/lysine phosphate hydrogen bonding. Fluorescence microscopic images (**c**), 3D reconstruction (**d**), quantitative analysis of ER/LD contact extent (**e**), and electron microscopic images (**f**) of WT CLSTN3B and RK mutant-mediated ER/LD contact in HEK293 cells. Scale bar: 5 µm in (**c**); 3 µm in (**d**); 200 nm in (**f**). Similar results have been obtained from at least 3 repeats for (**c**, **f**). Statistical significance was calculated by two-sided Wilcoxon test for (**e**). Source data are provided as a Source Data file.

alternative approach of digesting isolated LDs with proteinase K to remove bound ER followed by click-chemistry labeling of newly synthesized PC having translocated from the ER to LD (Fig. 6b and Supplementary Fig. 7b). This approach allowed clearer visualization and accurate quantitation of the LD monolayer phospholipids. The results again showed that LDs from CLSTN3B-expressing cells displayed significantly higher levels of labeled PC than control cells or cells expressing the RK mutant (Fig. 6e, f), supporting more efficient ER-to-LD phospholipid transfer under CLSTN3B expression.

To visualize CLSTN3B-mediated ER-to-LD phospholipid in live cells, we developed an approach to assess ER/LD phospholipid exchange rate by combining copper-free click chemistry labeling of newly synthesized PC with FRAP (Fig. 6g). We first labeled PC in U2OS cells with azide choline, induced LD formation in U2OS cells, and transfected cells with CLSTN3B-mCherry or RK mutant-mCherry constructs. At 12 hrs post-transfection, we performed copper-free clicking by treating cells with BDP FL DBCO, and immediately started FRAP. By simultaneously imaging the mCherry channel, we selected LDs incompletely wrapped by the ER to distinguish phospholipid signals exclusively from the LD monolayer versus those from closely juxtaposed LD and ER membranes. Whereas LDs in control cells showed negligible recovery within the experimental time frame, cells expressing WT CLSTN3B-mCherry displayed rapid recovery of LD monolayer phospholipid fluorescence after bleaching (Fig. 6h, i). The speed and extent of recovery was significantly diminished in cells expressing the RK mutant (Fig. 6h, i). We have therefore demonstrated CLSTN3B-mediated ER-to-LD phospholipid diffusion under a live cell setting.

To examine whether CLSTN3B-mediated ER-to-LD phospholipid diffusion could be recapitulated in a semi-reconstituted system,

we prepared microsomes from cells transfected with an empty vector, WT CLSTN3B or the RK mutant and labeled with alkyne choline. We first incubated those microsomes with LDs isolated from the BAT of *clstn3b*^{-/-} mice, a condition allowing CLSTN3B-mediated microsome/LD binding (Supplementary Fig. 7c, d). We then digested the LDs with proteinase K to remove bound microsomes and detected the presence of alkyne choline-containing PC on those LDs by click chemistry fluorescence imaging or thin layer chromatography (Fig. 6j–l and Supplementary Fig. 7e). Under this condition, microsomes from cells expressing WT CLSTN3B promoted significantly higher levels of phospholipid transfer to LDs than those from control cells or cells expressing the RK mutant. Taken together, our fixed cell imaging, live cell imaging, and semi-reconstituted assay data support that CLSTN3B facilitates ER-to-LD phospholipids diffusion, and this process requires optimal ER-LD contact formation driven by the arginine-rich segment.

## The arginine-rich region of CLSTN3B induces membrane hemifusion

We then directly tested the hypothesis that CLSTN3B-mediated ER-to-LD phospholipid diffusion occurs via the arginine-rich region-induced hemifusion-like structures between the ER cytosolic leaflet and the LD monolayer. For this purpose, we examined the ability of an CLSTN3B-derived arginine-rich peptide (CLSTN3B 222–232: RTRNLRPTRRR) to promote liposome hemifusion with a Fluorescence Resonance Energy Transfer (FRET)-based assay system (Fig. 7a)[45]. We observed that the arginine-rich peptide but not an RK mutant peptide promoted phospholipid mixing (Fig. 7b). The activity of the CLSTN3B-derived arginine-rich peptide exhibited a strong dose dependence on phosphatidic acid (PA) (Fig. 7c), an anionic conical phospholipid
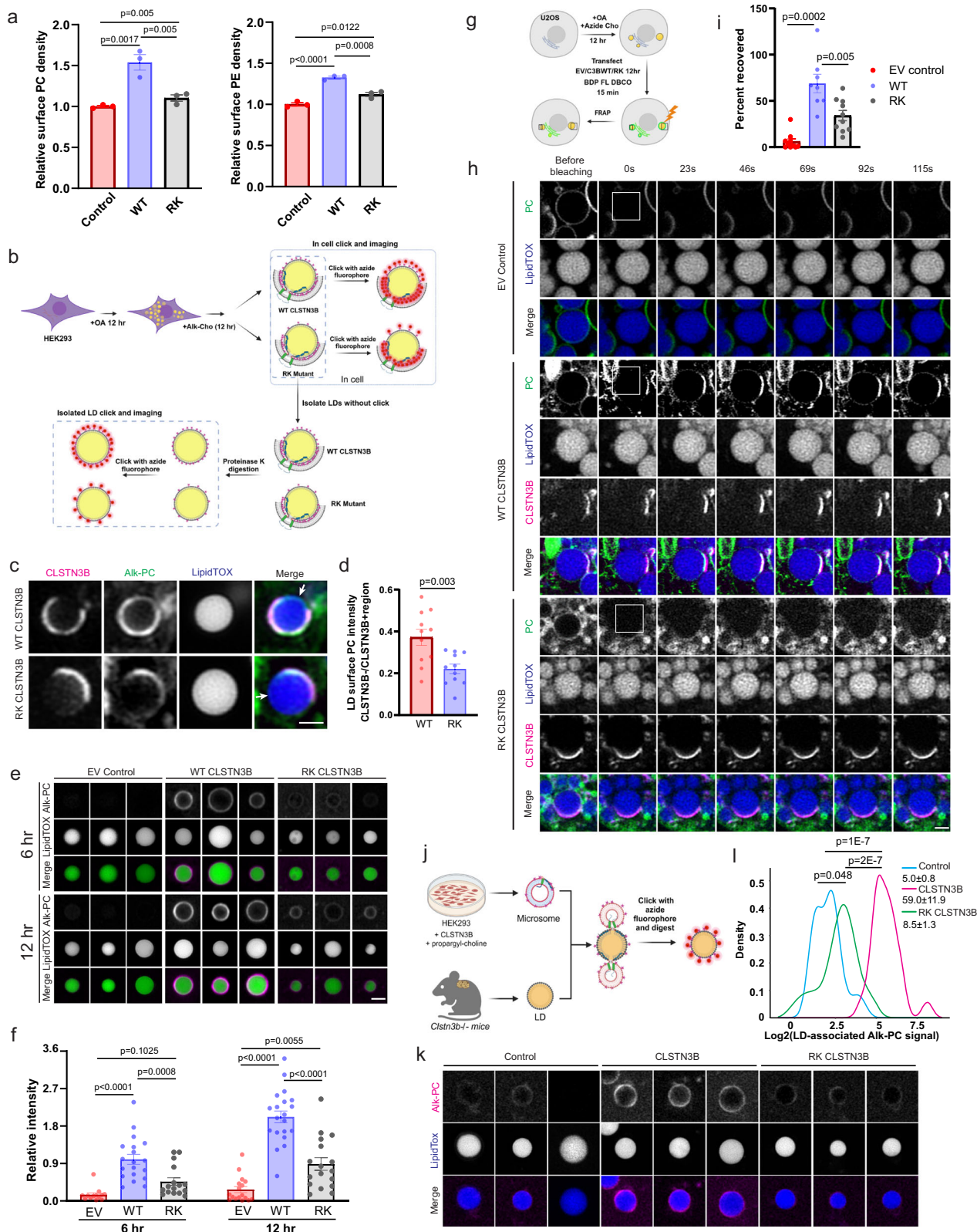
Fig. 6 | The arginine-rich region of CLSTN3B facilitates ER-to-LD phospholipid diffusion. a Fluorometric phospholipid quantitation of LDs isolated from empty vector, WT CLSTN3B or RK mutant-expressing HEK293 cells ($n = 3$ biological replicates). Schematics (**b**), representative images (**c, e**), and quantitation (**d, f**) of click-chemistry based ER-to-LD phospholipid transfer assay using fixed cell ($n = 11$) (**c, d**) or isolated LD ($n = 13$–20 LDs for each condition) (**e, f**). Scale bar: 1 μm. Schematics (**g**), representative images (**h**), and quantitation (**i**) of FRAP analysis of phospholipid exchange between ER and LD using copper-free click-chemistry labeled PC ($n = 8$–10 LDs for each condition). Scale bar: 1 μm. Schematics (**j**), representative images (**k**), and quantitation (**l**) of click-chemistry based semi-reconstituted phospholipid transfer assay. Scale bar: 2 μm. Data are mean ± s.e.m. Statistical significance was calculated by one-way ANOVA with Tukey's post hoc test for (**a, f, i, l**), and unpaired Student's two-sided t test for (**d**). Source data are provided as a Source Data file. **b, g**, and **j** were created in BioRender.
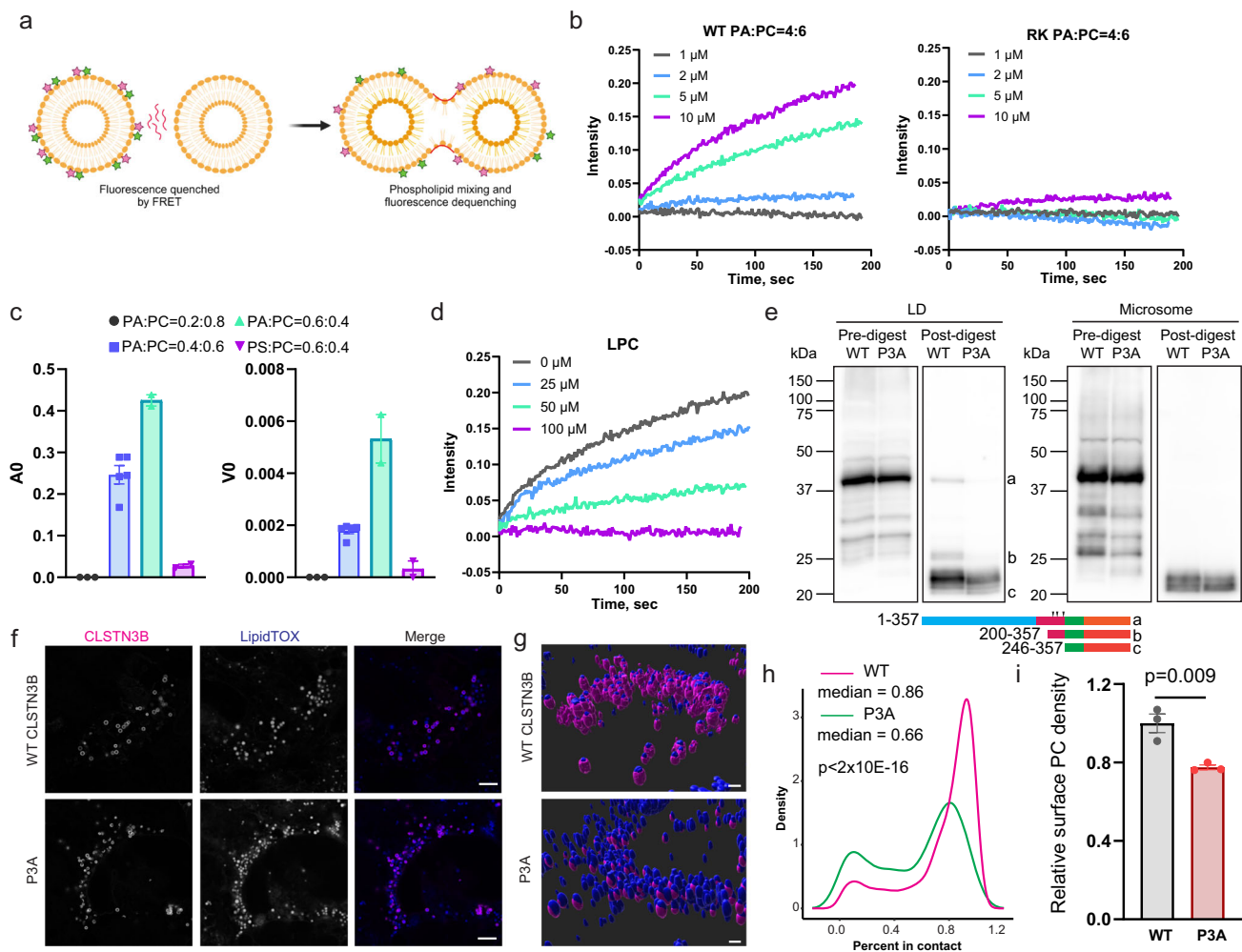
Fig. 7 | CLSTN3B promotes hemifusion-like structure formation. Schematics (**a**) of FRET-based detection of liposome lipid mixing induced by a CLSTN3B-derived R-rich peptide or a RK mutant peptide (**b**), the dependence on phospholipid composition for lipid mixing (n = 2–5 independent replicates) (**c**), and the effect of LPC on lipid mixing (**d**). **e** Western blot analysis of WT or P3A CLSTN3B fragments generated from trypsin digestion of LDs from HEK293 cells. The positions of fragments with defined lengths are shown as references (see also Extended Data Fig. 8e). Arrows denote positions of mutated prolines. Fluorescence microscopic images (**f**), 3D reconstruction (**g**), quantitative analysis of ER/LD contact extent (**h**), and measurement of LD surface PC levels (n = 3 biological replicates) (**i**) in WT CLSTN3B and P3A mutant-expressing HEK293 cells. Scale bar: 2 µm. Similar results have been obtained from at least 3 repeats for (**f**). Data are mean ± s.e.m. Statistical significance was calculated by two-sided Wilcoxon test for (**h**), and unpaired Student's two-sided *t* test for (**i**). Source data are provided as a Source Data file. **a** was created in BioRender.

favoring negative membrane curvature required for hemifusion stalk formation[46], but was antagonized by an inverse conical phospholipid lauroyl-lysophosphatidylcholine (LPC) (Fig. 7d), which favors positive membrane curvature and inhibits hemifusion[47]. These results strongly support a direct role of CLSTN3B in promoting ER-to-LD phospholipid diffusion via arginine-rich region-mediated formation of a hemifusion-like structure.

Prolines in the arginine-rich region are important for CLSTN3B function

Our model for CLSTN3B-supported membrane fusion at the ER/LD contact site predicts that the peptide backbone of the arginine-rich segment needs to sustain abrupt turns in accordance with the negative membrane curvature, given the extremely narrow space at the contact site (Supplementary Figs. 5c, d and 6a–f). This prediction is consistent with the abundant presence of proline residues in this region, given that prolines can adopt the *cis*-configuration and introduce bends in the peptide backbone. To test the significance of the proline residues, we mutated 3 prolines to analanines (P220, 228, 241A, or P3A). The P3A mutant was more susceptible to trypsin digestion than the WT

CLSTN3B on isolated LDs but not microsomes (Fig. 7e and Supplementary Fig. 7f), consistent with the arginine-rich region of the mutant not able to remain tightly associated with the curved membrane surface and more accessible for trypsin digestion. Functionally, the P3A mutant is less effective at promoting ER/LD contact formation and enhance LD surface phospholipid levels (Fig. 7f–i). Taken together, we have provided evidence supporting CLSTN3B-supported membrane fusion at ER/LD contact, with arginine residues required for interacting with phospholipids and proline residues contributing to the peptide backbone curvature.

CLSTN3B promotes LD maturation

Our model of CLSTN3B-mediated ER-to-LD phospholipid diffusion predicts that CLSTN3B may play a prominent role during LD growth to meet the phospholipid demand from the expanding LD surface, whereas its importance on mature LDs may be diminished. To examine whether this is the case, we investigated how endogenous CLSTN3B localization correlates with LD size in adipocytes. Indeed, we found more prominent CLSTN3B signals around small LDs in adipocytes, especially on the newly generated growing small LDs after

norepinephrine treatment (Fig. 8a, b). The signals are specific to endogenous CLSTN3B because they are completely absent in *clstn3b*⁻/⁻ adipocytes (Fig. 8a). Remarkably, even in *clstn3b tg* brown adipocytes expressing CLSTN3B at 7-fold higher than WT cells, CLSTN3B is still preferentially associated with small LDs (Fig. 8a). To understand the time-dependence of CLSTN3B association with growing LDs, we performed a NE treatment time-course. Before NE-treatment, brown adipocytes contained mostly large LDs with scanty CLSTN3B signal around them. After overnight NE treatment, numerous small growing LDs emerged with prominent CLSTN3B signal around them, which can be strongly inhibited by the long-chain acyl CoA synthetase inhibitor triacsin C, confirming those small LDs were generated de novo from re-esterified free fatty acids released after NE stimulation, consistent with previous observations[48,49]. On day 5 after NE withdrawal, all small LDs became large, accompanied by the disappearance of CLSTN3B signal (Fig. 8c–e). As an alternative approach, we analyzed CLSTN3B protein levels on LDs isolated from the BAT of cold-acclimated mice, which harbors many small growing LDs, or LDs from the BAT of warm-acclimated mice or the pgWAT, which contains only large mature LDs. Besides an overall reduction in CLSTN3B protein amount on large LDs, which can be partly accounted for by the lower mRNA expression levels of CLSTN3B in warm BAT or pgWAT as previously noted[26], the relative abundance of full-length CLSTN3B to a C-terminal fragment decreased substantially on large LDs compared with small LDs (Supplementary Fig. 7g). Taken together, our data showed that full-length CLSTN3B-mediated ER/LD contact preferentially occurs on newly formed small growing LDs but becomes profoundly diminished on large mature LDs, further supporting a role of CLSTN3B during LD maturation.

Lastly, we wanted to obtain direct functional evidence for CLSTN3B-mediated LD maturation, and the dependence on the arginine-rich segment. We measured time-dependent changes in LD sizes in HEK293 cells transfected with an empty vector, WT CLSTN3B, the RK or P3A mutant following OA treatment. LDs in cells expressing the WT CLSTN3B grew at a significantly faster rate than other conditions (Fig. 8f, g). These observations support our model that CLSTN3B promotes LD maturation via the arginine-rich segment-mediated ER/LD membrane fusion and phospholipid diffusion.

Discussion

We have elucidated that the mammalian adipocyte-specific protein CLSTN3B utilizes an arginine-rich segment to promote extensive ER/LD contact formation and facilitate ER-to-LD phospholipid diffusion via membrane fusion during the early phase of LD growth, which in turn allows better retaining of LD-targeting proteins as they are recruited to maturing LDs. LDs in adipocytes grow to uniquely large sizes and require a larger supply of surface structural molecules than in other cell types. Hence, CLSTN3B provides an adipocyte-specific mechanism to allow LDs to reach a high level of structural and functional maturity (Fig. 8h). In brown adipocytes, CLSTN3B enhances LD surface structure to reduce surface tension, prevents excessive LD coalescence to ensure sufficient LD surface area, and sensitizes lipolytic response to β-adrenergic stimulation, all beneficial to thermogenesis. In white adipocytes specializing in energy storage, CLSTN3B enhances the surface structure of the large monolocular LDs to protect the internal TG storage from unregulated lipolysis and allow them to undergo expansion in response to caloric overload. Overall, CLSTN3B allows LD size and function to become more polarized tailoring to the needs of distinct cellular contexts. The ability of CLSTN3B to simultaneously promote energy storage and efficient mobilization in response to body needs may have conferred mammals a survival advantage by increasing their adaptability to varying environmental conditions.

A common variant within the arginine-rich region of CLSTN3B exists in the human population (R224S) dictated by single nucleotide polymorphisms (SNPs) rs1868799 and 1868800. Since R224 falls within the arginine-rich region of CLSTN3B, it can be predicted based on our

model that the R224S variant represents a hypomorph of CLSTN3B. Interestingly, these SNPs and another tightly linked one rs7296261 have been shown to be associated with metabolic parameters, such as Body Mass Index (BMI) and Homeostatic Model Assessment for Insulin Resistance (HOMA-IR)[50]. Whether the apparent association can be explained by the impaired fusogenic activity of the R224S variant warrants further investigation.

It is interesting that the pgWAT of *clstn3b*⁻/⁻ mice on chow diet tends to be larger than the WT counterpart, the opposite of what we observed under the HFD condition. At first glance, this may seem inconsistent with the LD defects in *clstn3b*⁻/⁻ white adipocytes and the physiological evidence of impaired WAT lipid storage on chow diet. Curiously, we found that in the *clstn3b*⁻/⁻ pgWAT, the expression levels of genes in the DNL pathway and certain PPARG targets are significantly upregulated (Supplementary Fig. 1k, l). We think these gene expression changes may contribute to increased DNL in the pgWAT, which explains the larger pgWAT masses in *clstn3b*⁻/⁻ mice on chow diet. However, when the mice are challenged with HFD, their dramatic WAT expansion is predominantly driven by dietary fat intake. Furthermore, the strongly increased demand for lipid storage under the HFD condition helps reveal the *clstn3b*⁻/⁻ adipocytes' defective lipid storage capacity. Overall, CLSTN3B's role in perigonadal white adipocytes can be understood best as preparing those cells for storing lipids from external sources, achieved by a dual mechanism of strengthening LD structure and suppressing DNL. The mechanistic basis underlying CLSTN3B-mediated suppression of DNL in perigonadal white adipocytes represents a highly intriguing topic for follow-up investigations.

In contrast to the pgWAT, the inguinal subcutaneous WAT (scWAT) and the BAT in *clstn3b*⁻/⁻ mice are not significantly smaller than the WT counterparts under the HFD condition. This discrepancy can be at least partly explained by reduced lipid mobilization in the BAT and scWAT of *clstn3b*⁻/⁻ mice resulting from defective sympathetic innervation, opposing the effect of impaired tissue expandability due to LD defects. Indeed, both the BAT and the scWAT receive significantly higher levels of parenchymal sympathetic innervation than the pgWAT[28], supporting the notion that defective sympathetic innervation will likely have a larger impact on lipid mobilization in the BAT and the scWAT than the pgWAT.

Although a previous report suggested an antagonism between CLSTN3B and CIDE-protein activity in brown adipocytes, our findings indicate that CLSTN3B and CIDE-proteins work cooperatively in the context of lipid storage in the pgWAT. Previously published loss-of-function and gain-of-function models all support a pro-lipid storage function of CIDE-protein in the WAT[34–36]. Our complete set of mouse models encompassing global KO, pan-adipocyte/brown adipocyte-selective conditional KO, and transgenic models demonstrated an unequivocal function of CLSTN3B in promoting lipid-storage in the pgWAT. Rather than antagonizing CIDE-proteins, our findings suggest that CLSTN3B works in the same direction as CIDE-proteins in white adipocytes. Indeed, CIDEA and CIDEC were found to be among the most strongly downregulated proteins on LDs from *clstn3b*⁻/⁻ white and brown adipocytes (Fig. 4d, e), suggesting that CLSTN3B may enhance CIDE-protein stability. CIDEA is known to be an unstable protein susceptible to ubiquitination and proteolysis[51]. A direct interaction between CLSTN3B and CIDE-proteins as reported previously would explain CLSTN3B-mediated CIDE-protein stabilization[27]. Nevertheless, we showed that CIDEA, along with multiple known LD surface proteins, is excluded from full-length CLSTN3B-mediated ER/LD contact, raising questions about where and how the reported CLSTN3B/CIDEA interaction may happen. Interestingly, we detected multiple forms of CLSTN3B present on LDs (Supplementary Fig. 7g), suggesting an intriguing scenario that CLSTN3B may be processed into fragments, with each fragment possessing unique functions. For example, whereas full-length
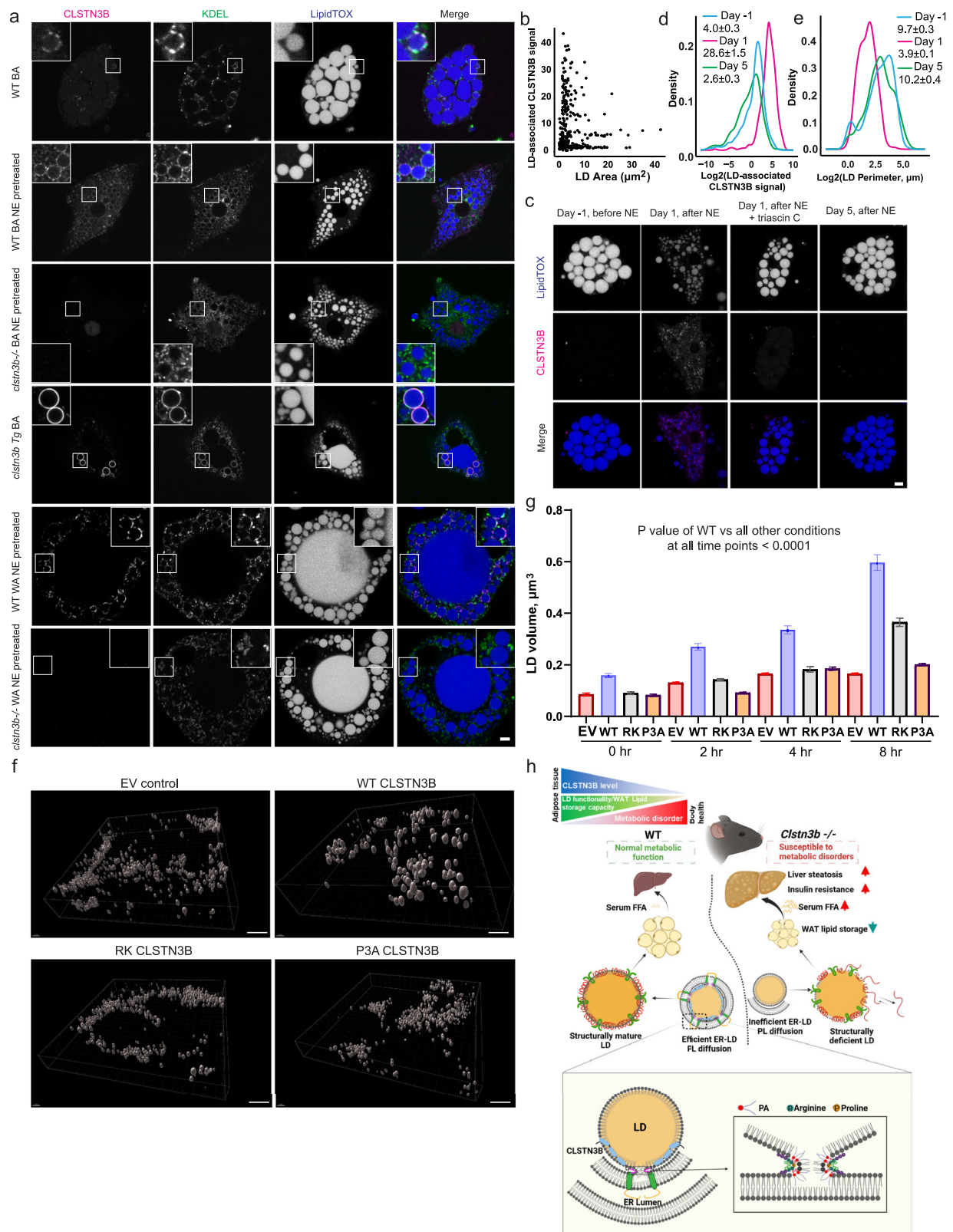
Fig. 8 | CLSTN3B promotes LD maturation. a Fluorescence microscopic analysis of CLSTN3B and KDEL localization in primary adipocytes. Scale bar: 5 μm. **b** Relationship between LD-associated CLSTN3B intensity and LD size. **c** Fluorescence microscopic analysis of CLSTN3B localization in primary brown adipocytes over a NE-treatment time course. Scale bar: 5 μm. Quantitation of LD-associated CLSTN3B signal intensity (**d**) and LD size (**e**) in (**c**). Fluorescence microscopic images (**f**) and quantitative analysis (**g**) of LD sizes in HEK293 cells transfected with empty vector (EV), WT CLSTN3B, RK CLSTN3B, or P3A CLSTN3B at indicated time points after OA treatment ($n = 200$–2000 LDs for each condition). Scale bar: 5 μm. **h** Model of CLSTN3B action at the molecular, organellar, cellular and organismal levels. Similar results have been obtained from at least 3 repeats for (**a**, **c**). Data are mean ± s.e.m. Statistical significance was calculated by one-way ANOVA with Tukey's post hoc test for (**g**). Source data are provided as a Source Data file. **h** was created in BioRender.

CLSTN3B may be primarily responsible for inducing ER/LD contact on small growing LDs, an LD-residing fragment may be involved in stabilizing CIDE-proteins on mature LDs no longer in extensive association with the ER. This model is consistent with how the relative abundance of multiple forms of CLSTN3B varies between small and large LDs. Further studies are required to reveal the mechanistic details underlying the CLSTN3B/CIDE-protein interaction, its relevance to CIDEA turnover, and clarify the existence and potential function of various CLSTN3B fragments.

The selective presence of full-length CLSTN3B and ER contact on small LDs in their early growth phase raises three important questions: how CLSTN3B-mediated ER/LD contact and membrane bridge is initiated with CLSTN3B originally residing in the ER; how the membrane bridge gets resolved to allow ER detachment from mature LDs; whether CLSTN3B continues to facilitate phospholipid replenishment on mature LDs. A recent study showed the membrane fusion machinery induces membrane bridge formation between the ER exit site and LD[25]. We speculate that such membrane bridges could provide an initial route for the N-terminal LD-targeting domain of CLSTN3B to relocate from the ER onto the LD surface. Once in place, CLSTN3B can use its unique arginine-rich region to induce additional membrane fusion and promote extensive ER/LD contact. Importantly, multiple proteins involved in membrane fusion, namely certain RABs and the TRAPPC subunits, that were identified by Song et al.[25], were also found to be downregulated on LDs from clstn3b^{-/-} adipocytes, supporting our model that CLSTN3B may reinforce or stabilize the membrane bridge initiated by the RAB/TRAPPC machinery. The presence of short forms of CLSTN3B in the ER suggests an intriguing possibility that proteolysis may be involved in the ER/LD separation process as LDs mature, whereas the competition between LD-targeting proteins, such as PLIN1 and CIDEA, and CLSTN3B may also reduce the ER/LD contact area as LDs expand. Lastly, our proteomics results suggest that CLSTN3B may continue to facilitate phospholipid replenishment to mature large LDs via ER-derived vesicles or caveolae, given the significant downregulation of the vesicle fusion-related proteins and caveolae proteins specifically on LDs from clstn3b^{-/-} white adipocytes. Interestingly, caveolae ablation results in a similar phenotype of WAT expansion defects to clstn3b^{-/-} mice[52,53]. Follow-up investigations are required to clarify the role of RABs, their cognate GEFs, and caveolae in supporting CLSTN3B function on large mature LDs.

Methods

All animal studies were approved by and in full compliance with the ethical regulation of the Institutional Animal Care and Use Committee (IACUC) of University of Texas Southwestern Medical Center. Mice were euthanized by CO2 asphyxiation, according to the guidelines of IACUC and the recommendations of the Panel on Euthanasia of the American Veterinary Association.

Mouse strains

The clstn3b^{-/-} and the adipose-specific clstn3b transgenic mice were described in a previous publication Zeng et al[26]. Mice were maintained on a normal chow diet (13% fat, 57% carbohydrate and 30% protein, PicoLab Rodent Diet 5L0D) and/or placed on a high-fat diet (HFD, Rodent diet with 60 kcal% Fat, Research diet, D12492, USA) from 6−8 weeks of age for 8 to 14 weeks. All mice were maintained under a 12 hr light/12 hr dark cycle at constant temperature (23 °C or 30 °C as specified) and 40−60% humidity with free access to food and water. The clstn3b floxed mouse was generated at the transgenic core at University of Texas Southwestern Medical Center. Two gRNAs (CCCCAGCAGGAAGTGTAAAC; ATGGCCCCGTGGCTAAGCCC) flanking exon 1 of clstn3b and a donor HDR long ssDNA template encompassing exon1 and two loxP sites were synthesized by Sythego and Azenta respectively. The gRNAs were mixed with CAS9 protein from IDT to form a ribonucleotide protein complex. The ssDNA HDR template was added to the mix and the cocktail was microinjected into the pronucleus of fertilized one-cell eggs isolated from superovulated females with concentration CAS9 25 ng/μL, gRNA concentration of 25 ng/μL and ssDNA template 8 ng/μL. The eggs were incubated in media containing cytochalasin-B immediately before and during microinjection to improve egg survival. The surviving eggs were transferred into the oviducts of day 0.5 pseudopregnant recipient ICR females (Envigo, Inc.) to produce putative founder mice. The correct insertion of the loxP sites was verified by PCR. All animal studies were approved by and in full compliance with the ethical regulation of the Institutional Animal Care and Use Committee of University of Texas Southwestern Medical Center. Sample size was chosen based on literature and pilot experiment results to ensure that statistical significance could be reached. Randomization was not performed because mice were grouped based on genotype. Littermates were used for all the experiments involving the conditional KO and transgenic mice. The global clstn3b^{-/-} mice were maintained as a homozygous cohort. The WT control mice were either bred in-house or purchased from vendors and, in the latter case, acclimated in the same environment as the global clstn3b^{-/-} mice for at least two weeks prior to the start of the experiment.

Reagents

FFA fluorometric assay kit (Cayman, item no.700310); Lipofectamine 3000 (Invitrogen, L3000-015); Norepinephrine (Sigma, A9512); HCS LipidTOX™ Deep Red Neutral Lipid Stain (Invitrogen™, H34477); HCS LipidTOX™ Green Neutral Lipid Stain (Invitrogen™, H34477); Trypsin Platinum (Promega, VA9000); Protease K (Sigma, P2308); Oleic acid (Sigma, O1383); BSA (Sigma, A7030); FFA-free BSA (Millipore, Code82-002-4); Trypsin inhibitor (Worthington, LS003571); Protease inhibitor cocktail (100X) (Thermo scientific, 1861279); Free glycerol reagent (Sigma, F6428-40ML); Propargyl choline (Cayman, 25870); BTTAA (Click chemistry tools, 1236-100); CalFluor 647 Azide(Click chemistry tools, 1272-1); Phosphatidylcholine Assay Kit (Colorimetric/Fluorometric) (Abcam, ab83377); Phosphatidylethanolamine Assay Kit (Fluorometric) (Sigma, MAK361).

Antibody: CLSTN3B antibody was described previously Zeng et al[26]; KDEL (Abcam, ab184819); PLIN1 (Abcam, ab3526); CGI-58 (Abcam, ab183739); UCP1(Abcam, ab209483); PDI (Cell signaling, C81H6); CS (Abcam, ab129095). Seipin (Cell signaling, 23846S), HA-tag (Cell signaling, 3724S), FLAG (Sigma, F1804), PLIN1 (Cell signaling, 9349S), p-HSL(s660) (Cell signaling, 4126), HSL (Cell signaling, 4107S), Alexa Fluor 546 Fluor Nanogold IgG goat anti-mouse (Nanoprobes, 7410-1 ML), Alexa Fluor 488 Fluor goat anti-Rabbit (Invitrogen, A11034), Alexa Fluor 564 Fluor goat anti-mouse (Invitrogen, A11030), Alexa Fluor 405 Fluor goat anti-rabbit (Invitrogen, A31556).

Constructs: PCDNA3.1-clstn3b was described previously[15]; clstn3b-mCherry, clstn3b(1-131)-mCherry, clstn3b(1-198)-mCherry, clstn3b(131-357)-mCherry, clstn3b(199-357)-mCherry, seipin, and clstn3b-C1-FLAG were synthesized by Gene Universal Inc. (Newark DE 19713); BFP ER-reporter was purchased from Addgene (49150).

HEK293A cells were obtained from CELL BIOLABS (AD100). HeLa (CRM-CCL-2) and U2OS (HTB-96) Cells were obtained from ATCC.

Electron microscopy

Primary adipocytes were isolated as previously described and allowed to attach to MatTek glass bottom grid dishes (P35G-1.5-14-CGRD) Zeng et al[26]. The cells were treated with 1 μM norepinephrine overnight to induce the formation of small LDs when specified. Cells were then fixed with 4% paraformaldehyde + 0.1% glutaraldehyde in PBS containing 7.5% sucrose for 30 min at RT, blocked with 50 mM glycine for 15 min, permeabilized with 0.25% saponin for 30 min. Cells were than incubated with the CLSTN3B antibody at 4 °C overnight and then with the fluoronanogold secondary antibody (Nanoprobes 7403-1) for 2 h at RT. Images for taken on a Zeiss 900 confocal microscope to identify

the coordinates of the cells for EM analysis. The cells were further gold-enhanced for 2.5 min using a gold enhancement kit (Nanoprobes). After washing with water and 0.1 M cacodylate buffer, samples were fixed with 1% OsO4 and 0.8% potassium ferricyanide in 0.1 M cacodylate buffer for 1 h, stained en bloc with 2% aqueous uranyl acetate, dehydrated with increasing concentration of ethanol, and embedded in Epon. Blocks were sectioned with a diamond knife (Diatome) on a Leica Ultracut 7 ultramicrotome (Leica Microsystems) and collected onto copper grids. Images were acquired on a JOEL 1400 Plus transmission electron microscope equipped with a LaB6 source using a voltage of 120 kV, and the images were captured by an AMT BIOSPRINT 16M-ActiveVu mid mound CCD camera.

Glucose tolerance test

Mice (male, 8–10-week-old) were put on an HFD at thermoneutrality. For the WT and *clstn3b*^{-/-} cohorts, mice were maintained on the HFD for 8–10 weeks. For the WT and *clstn3b tg* cohorts, mice were maintained on the HFD for 12–14 weeks. No statistically significant difference in body weights between the comparison groups was observed at the time of the test. Prior to the start of GTT, mice were fasted for 16 h with free access to drinking water. Glucose (1.5 g/kg) was administered intraperitoneally, and blood glucose levels were measured with a Contour next EZ glucose monitor (Ascensia Diabetes Care, Parsippany, NJ 07054, United States) at 0, 15, 30, 60, 90, and 120 min. Body weight data are provided in the Source Data file.

AAV injection

Six-week-old male mice were anaesthetized with isoflurane and an incision was made above the interscapular area to expose the underlying BAT. About 3×10^{11} AAV particles were injected into each BAT lobe and the incision was closed with suture. Mice received one injection of meloxicam (2 mg/kg) 24 h before surgery, and another injection immediately after surgery. Mice were allowed to recover for three weeks and then treated with HFD for 12 weeks at thermoneutrality (30 C). AAV8-EF1a-DIO-Clstn3b was described as in Zeng et al.[26]

Liver TG and serum FFA measurement

Liver and serum samples were collected from WT and *clstn3b*^{-/-} cohorts or WT and *clstn3b tg* cohorts maintained on HFD at thermoneutrality. The HFD feeding scheme is described in the GTT section. About 60 mg of liver was removed from each mouse for measuring TG. TG levels were measured with the Triglyceride Colorimetric Assay Kit (Cayman, 10010303) or Glycerol Assay Kit (Sigma, MAK117) following the manufacturer's instructions. Serum FFA levels were measured with the Free fatty acid fluorometric assay kit (Cayman, 700310) following the manufacturer's instructions.

Fixed cell imaging

Primary adipocytes were isolated as previously described and attached to glass coverslips pre-coated with laminin and poly-D-lysine Zeng et al.[26] HEK293 cells and U2OS cells were plated onto glass coverslips and treated with 400 μM oleic acid for 12–24 hr to induce LD formation. Images were taken on a ZEISS 900 confocal microscope with Airyscan.

Image analysis

To analyze isolated lipid droplets, images were imported to Imaris (Bitplane). Individual LDs were rendered by the "Surface" function and surface area and volume were measured. The rendering parameters were kept the same between treatments in each experiment. To analyze the extent of CLSTN3B wrapping of LDs, individual LDs and the surrounding CLSTN3B signals were rendered by the "Surface" function. The fraction of the volume bound by the LD surface overlapping with the volume bound by the CLSTN3B signal surface was calculated

with the "Object-Object statistics" function. To analyze LD-associated signals (PC, microsomes, KDEL, CLSTN3B or PLIN1), images were imported to ImageJ (NIH). Individual LDs were detected by the "Analyze particle" function, and a larger ROI was generated for each LD via the "Dilate" function to encompass surrounding signal of interest. Fluorescence signal intensity associated with LDs was then measured, normalized or transformed, and plotted. To analyze ER wrapping of LD in EM images, the LD perimeter and the fraction in contact with the ER are selected and calculated with the polygon tool in Image J. To analyze ER lumen width in EM images, a line is drawn through the lumen and perpendicular to the ER membrane and the length of the line is calculated in Image J. All plots were generated in R.

LD isolation and digestion

For BAT LD, BAT was dissected, minced into tiny pieces with a spring scissor and transferred to a motorized homogenizer in HES buffer (20 mM HEPES + 1 mM EDTA + 250 mM Sucrose). The homogenate was filtered with double-layer gauze and centrifuged at 2000 g for 5 min. The infranatant was removed with a syringe and the buoyant LD fraction was transferred with a wide-opening tip into 5 ml tubes and washed with HES buffer 2 times. The LD was then transferred to Ultra-Clear ultracentrifuge tubes (Beckman-Coulter), adjusted to a final concentration of 20% sucrose, and overlaid by 5% sucrose/HE and HE (20 mM HEPES + 1 mM EDTA). The gradient was centrifuged at 16,000 g for 10 min at 4°C. The buoyant LD was then collected.

For WAT LD, WAT was dissected, minced into tiny pieces with a spring scissor and transferred to digestion buffer. Digest on a rotator at 37°C for 30 min. Filter with 100um cell strainer into a 50 mL tube. (Digest buffer: HBSS + 2 mg/ml Collagenase B + 1 mg/ml Trypsin inhibitor + 4% BSA (FA free) + 25U/ml Benzonase (1:10000)). Transfer the cell suspension to a 5 mL tube and wash with HES buffer 3 times. Disrupt the cell in HES buffer by gently passing through a 25 G needle with 10 times. Wash 3 times with HES buffer. Don't centrifuge or vortex, let it stand for 10 min until the buoyant LD fraction float to the upper layer. Keep the buoyant LD fraction. For measuring the PL of WAT LD, transfer the LD fraction to Ultra-Clear ultracentrifuge tubes (Beckman-Coulter), diluted to a final concentration of 20% percoll. Centrifuge 10000 g X 20 min at 4°C, keep the buoyant LD fraction.

For HEK293 LD, 15-cm dishes of HEK293 cells were grown to 90% of confluence and treated with 400 μM oleic acid in growth medium for 24 h. Cells were scraped and collected in 2 mL of lysis buffer (25 mM Tris−HCl, pH 7.4, 100 mM KCl, 1 mM EDTA, 5 mM EGTA, and protease inhibitor cocktail), and lysed by passing through a needle (27-gauge). The lysates were then centrifuged at 1,500 g for 5 min. The supernatants were adjusted to 2.5 mL final volume containing 20% sucrose and transferred into a 10 mL polycarbonate ultracentrifuge tube, and overlaid sequentially with 2.5 mL of 10% sucrose, 2.5 mL of 4.2% sucrose, and 2.5 ml of lysis buffer. The gradient was centrifuged at 150,000 g for 1 hr at 4°C. The buoyant LD was then collected.

For topology determination, LDs isolated from BAT were incubated with trypsin (50 μg/ml, Promega) for 30 min, followed by centrifuging LD fractions through the aforementioned sucrose gradient at 210,000 g for 1 hr. The buoyant LD fraction and the pellet fraction were collected separately.

To remove the LD-bound organelles, the LD fraction was digested with 1 mg/mL proteinase K for 5–15 min at 37 °C and 1 mM PMSF was added to inactivate proteinase K. The mixture was centrifuged through the aforementioned sucrose gradient at 210,000 g for 1 hr. The buoyant LD was then collected.

Immunoprecipitation

HEK293 cells were transfected with the indicated plasmids After 48 h, cells were washed once with PBS, resuspended in lysis buffer (25 mM Tris-HCl pH 8.0, 150 mM NaCl and 1× protease inhibitor cocktail), and

homogenized with a motorized homogenizer. The lysate was then supplemented with 1% digitonin, incubated on rotator at 4 °C for 2 hr, and centrifuged at 20,000 g for 15 min at 4 °C. FLAG-tagged protein was isolated with anti-FLAG M2 magnetic beads (Sigma, M8823) for 2 hr at 4 °C and eluted with 100 µg/ml 3x FLAG peptide.

Proteomics

LD was isolated from mouse BAT or WAT as described above without protease digestion. The suspension was mixed with 10x volume of acetone and incubated at −20°C overnight for delipidation and protein precipitation. The mixture was centrifuged at 12,000 g for 5 min. The pellets were washed with acetone and dried by heating at 60°C for at least 15 min. Pellets were then washed with 20% TCA to remove excess sucrose, washed with acetone, and dried. The pellets were dissolved in 50 mM triethylammonium bicarbonate (TEAB, pH=8), 5% SDS at 60°C with shaking for 30 min. Protein concentration was determined with a BCA method.

Samples were then reduced by adding dithiothreitol (DTT) to a final concentration of 10 mM and samples were incubated at 56 °C for 30 min. After cooling, iodoacetamide was added to a final concentration of 20 mM and samples were alkylated for 30 min at room temperature in the dark. Following centrifugation for 2 min at 13.2 krpm, the supernatants were removed and digested overnight with trypsin at 37 °C using an S-Trap (Protifi). Following digestion, the peptide eluate was dried and reconstituted in 100 mM TEAB buffer. The samples were labeled with TMT10plex reagents, quenched with 5% hydroxylamine, and combined. For the BAT LD samples, the WT replicates were labeled with TMT labels 126, 127 C, 127 N, and 128 N, while the KO replicates were labeled with 128 C, 129 N, 129 C, and 130 N. For the WAT LD samples, the WT replicates were labeled with TMT labels 126, 127 C, 127 N, 128 C, and 128 N, while the KO replicates were labeled with 129 C, 129 N, 130 C, 130 N, and 131. The mixed samples were dried in a SpeedVac and reconstituted in a 2% acetonitrile, 0.1% TFA buffer to a final concentration of ~0.5 ug/uL based on NanoDrop A205 (Thermo).

Samples were injected onto an Orbitrap Fusion Lumos mass spectrometer coupled to an Ultimate 3000 RSLC-Nano liquid chromatography system (Thermo). Samples were injected onto a 75 um i.d., 75-cm long EasySpray column (Thermo) and eluted with a gradient from 0–28% buffer B over 180 min. Buffer A contained 2% (v/v) ACN and 0.1% formic acid in water, and buffer B contained 80% (v/v) ACN, 10% (v/v) trifluoroethanol, and 0.1% formic acid in water. The mass spectrometer operated in positive ion mode with a source voltage of 1.8–2.0 kV and an ion transfer tube temperature of 300 °C. MS scans were acquired at 120,000 resolution in the Orbitrap and top speed mode was used for SPS-MS3 analysis with a cycle time of 2.5 s. MS2 was performed with CID with a collision energy of 35%. The top 10 fragments were selected for MS3 fragmentation using HCD, with a collision energy of 55%. Dynamic exclusion was set for 25 s after an ion was selected for fragmentation.

Raw MS data files were analyzed using Proteome Discoverer v2.4 SP1 (Thermo), with peptide identification performed using a trypsin digest search with Sequest HT (cleavage after Lys and Arg except when followed by Pro). The mouse reviewed protein database from UniProt (downloaded Jan. 28, 2022, 17,062 entries) was used. Fragment and precursor tolerances of 10 ppm and 0.6 Da were specified, and three missed cleavages were allowed. A minimum peptide length of 6 residues was required. Carbamidomethylation of Cys and TMT10plex labeling of N-termini and Lys sidechains were set as a fixed modification, with oxidation of Met set as a variable modification. The false-discovery rate (FDR) cutoff was 1% for all peptides. At least two unique peptides were required for protein identification.

Phospholipids quantitation

LD was isolated from mouse BAT, WAT or HEK293 cells and digested with proteinase K following the procedure described above. The collected LD fractions (100–200 µL suspension in HES buffer) were transferred into round bottom glass tubes and extracted with a mixture of 1 mL hexane, 1 mL methyl acetate, 0.75 mL acetonitrile and 1 mL water as previously described. The extracts were vortexed for 5 s and centrifuge at 2,671 g for 5 min to partition into 3 phases. The upper and middle phases were collected into separate glass tubes and dried under N_2. Phospholipids in the middle phase were measured with the Phosphatidylcholine Assay Kit (Colorimetric/Fluorometric) (Abcam, ab83377) and Phosphatidylethanolamine Assay Kit (Fluorometric) (Sigma, MAK361) following the manufacturer's instructions. TG in the upper phase was dissolved in 350 µL ethanolic KOH (2 part EtOH and 1 part 30% KOH) and incubated overnight at 55 °C for complete hydrolysis. The volume was then brought to 1200 µL with H2O: EtOH (1:1) and vortexed to mix. Two hundred µL was transferred to a new tube, mixed with 215 µL 1 M $MgCl_2$ and vortexed. The mixture was incubated on ice for 10 min and centrifuged at 13,000 g for 5 min. Glycerol content in the supernatant was determined with the Free Glycerol Reagent (Sigma, F6428) following the manufacturer's instructions.

For phospholipidomics analysis, a 50 µL aliquot of LD suspension was transferred to fresh glass tubes for liquid-liquid extraction (LLE). LLE were performed at room temperature (including centrifugation) to maintain consistent solubility and phase separation. For the three-phase lipid extractions (3PLE), 1 mL of hexanes, 1 mL of methyl acetate, 0.75 mL of acetonitrile, and 1 mL of water were added to the glass tube containing the sample. The mixture was vortexed, then centrifuged at 2,671×g for 5 min, resulting in separation of three distinct liquid phases. The middle organic phase (polar lipid content) was collected in a separate glass tube with a Pasteur pippete and spiked with 20 µL of a 1:5 diluted SPLASH Lipidomix standard mixture. The samples were dried under N_2 air flow and resuspended in 400 µL of hexane. Lipids were analyzed by LC-MS/MS using a SCIEX QTRAP 6500+ (SCIEX, Framingham, MA) equipped with a Shimadzu LC-30AD (Shimadzu, Columbia, MD) high-performance liquid chromatography (HPLC) system and a 150×2.1 mm, 5 µm Supelco Ascentis silica column (Supelco, Bellefonte, PA). Samples were injected at a flow rate of 0.3 mL/min at 2.5% solvent B (methyl tert-butyl ether) and 97.5% Solvent A (hexane). Solvent B was increased to 5% over 3 min and then to 60% over 6 min. Solvent B was decreased to 0% during 30 sec while Solvent C (90:10 (v/v) isopropanol-water) was set at 20% and increased to 40% during the following 11 min. Solvent C is increased to 44% over 6 min and then to 60% over 50 sec. The system was held at 60% solvent C for 1 min prior to re-equilibration at 2.5% of solvent B for 5 min at a 1.2 mL/min flow rate. Solvent D [95:5 (v/v) acetonitrile-water with 10 mM Ammonium acetate] was infused post-column at 0.03 ml/min. Column oven temperature was 25 °C. Data was acquired in positive and negative ionization mode using multiple reaction monitoring (MRM). The LC-MS/MS data was analyzed using MultiQuant software (SCIEX). The identified lipid species were normalized to its corresponding internal standard. All solvents used were either HPLC or LC/MS grade and purchased from Sigma-Aldrich (St Louis, MO, USA). Splash Lipidomix standards were purchased from Avanti (Alabaster, AL, USA). All lipid extractions were performed in 16×100 mm glass tubes with PTFE-lined caps (Fisher Scientific, Pittsburgh, PA, USA). Glass Pasteur pipettes and solvent-resistant plasticware pipette tips (Mettler-Toledo, Columbus, OH, USA) were used to minimize leaching of polymers and plasticizers.

To calculate LD surface phospholipids density, we divided phospholipids abundance as measured by the fluorometric kit or phospholipidomics by total LD surface area of each sample. To calculate total LD surface area, we divided total TG content of each sample by the mean LD volume to derive total LD number, which is then multiplied by the mean LD surface area. Mean LD volume and surface area were determined by analysis of LD images as described above. The entire process is summarized in Extended Data Fig. 4b.

In vitro reconstitution of CLSTN3B-mediated ER/LD contact formation and phospholipids transfer

To reconstitute CLSTN3B-mediated ER/LD contact formation, HEK293 cells were transfected with the *clstn3b*-mCherry or the BFP-ER reporter and cultured for 48 hr. Then cells were washed with warm PBS twice, scraped off, and lysed by passing through a 27 G needle 10 times. The lysates were centrifuged at 1000 g for 10 min to remove nuclei and cell debris. The supernatants were centrifuged through the aforementioned sucrose gradient at 210,000 g for 1 hr. The microsome pellets were suspended in the assay buffer (25 mM HEPES, 150 mM NaCl, 10 mM MgCl$_2$, 1 mM CaCl$_2$, 1 mM ATP, 0.5 mM GTP). LDs were harvested from and a parallel batch of HEK293 cells treated with 400 µM oleic acid in growth medium for 24 hr as described above. LDs and microsome suspension were then mixed and incubated at 37 ˚C overnight. The mixture was stained with HCS LipidTOX™ Green Neutral Lipid Stain (1:200) for 15 min and imaged on a ZEISS 900 confocal microscope. To reconstitute CLSTN3B-mediated phospholipids transfer, HEK293 cells were transfected with the *clstn3b*-mCherry, RK-*clstn3b*-mCherry, SEIPIN-HA or the BFP-ER reporter construct for 24 hr and then treated with 100 µM propargyl-choline for 12–24 hr. Microsome suspension was prepared as described above. LDs isolated from *clstn3b*$^{-/-}$ mouse BAT was incubated with the microsome suspension on a RotoFlex (Argos, R2200) set at a low speed at RT for 12 hr or overnight. The mixture was then centrifuged at 100 g for 5 min. The buoyant LD fraction was collected and incubated with the click reaction solution (50 µM Calfluo647 azide, BTTAA-CuSO4 complex (50 mM CuSO4, BTTAA/CuSO4 6:1, mol/mol) and 2.5 mM sodium ascorbate) for 1 hr at RT. The LDs were then digested with 1 mg/mL protease K for 5 min, treated with 1 mM PMSF for 5 min, and centrifuged at 100 g for 5 min. The buoyant LD fraction was stained with HCS LipidTOX™ Green Neutral Lipid Stain (1:200) for 15 min. Images were then taken on a ZEISS LSM 900 confocal microscope.

In vivo ER-to-LD phospholipid transfer assay

HEK293 cells were transfected with WT-CLSTN3B-mCherry, RK-CLSTN3B-mCherry, or an empty pCDNA3.1 vector for 24 hrs and then treated with 400 µM oleic acid in growth medium for 24 hrs. To label newly synthesized PC, the growth medium was supplemented with 200 µM propargyl-choline for 6 and 12 hrs, respectively. Lipid droplets were isolated at those time points, digested with proteinase K to remove bound ER, labeled with Calfluo647 azide, and imaged as described above.

Copper-free click chemistry phospholipid labeling and FRAP

U2OS was cultured for 12 h and then treated with OA (300 µM) and azide choline (50 µM) for 12–24 h to allow LD formation. The cells were then washed with PBS twice and transfected with pCDNA3.1 (empty vector), CLSTN3B-mCherry, or RK-mCherry overnight or 12 hrs. The short duration was used to restrict CLSTN3B expression and prevent complete ER wrapping around LDs. The cells were washed with PBS twice and incubated in serum-free DMEM with BDP FL DBCO (100 nM) for 15 min. The cells were then washed with fresh growth medium and allowed to sit for 60 min before the start of imaging. Regions of interest were bleached by 100% laser power (488 diode laser), followed by time-lapse imaging with a 23 sec interval. The fluorescence intensity of BDP FL DBCO on the LD monolayer was quantitated by ImageJ.

Lipolysis assay

Lipolysis assay on freshly isolated primary white and brown adipocytes were performed as previously described (Chen et al, PMID: 28988768). To measure the whole-body response to CL-316,243, mice were put under isoflurane anesthesia and i.p. injected with CL-316,243 at 1 mg/kg. Blood samples were collected from tails at 0- and 10-min. Serum FFA levels were measured with the Free fatty acid fluorometric assay kit (Cayman, 700310) following the manufacturer's instructions.

Liposome preparation

Large unilamellar vesicles (LUV) were prepared as described before (Yang et al., Biophys. J., 2010). Lipid mixtures dissolved in a benzene/methanol mixture (9:1 ratio) were frozen in liquid nitrogen and freeze-dried overnight in a CentriVap vacuum concentrator (Labconco, USA). The dried lipid was then resuspended in a buffer (100 mM NaCl, 10 mM Hepes, 5 mM EGTA, pH 7.0) at total lipid concentration of 1 mM. Subsequently, the lipid suspension underwent 10 freeze-thaw cycles by alternating immersion in liquid nitrogen and a 50 ℃ water bath. Finally, the suspension was passed ten times through the double-stacked nucleopore polycarbonate track etch membrane filters with a nominal pore size of 0.1 µm using a Lipex liposome extruder.

Lipid mixing experiments

Lipid mixing was measured by the release of fluorescence resonance energy transfer between TopFluor PE (0.5 mol %) and rhodamine PE (0.25 mol %). Unlabeled liposomes of various lipid compositions and liposomes labeled with a self-quenching concentration were added to 2 mL of buffer in quartz cuvette in a ratio of 10:1 to a total lipid concentration of 10 µM. Different concentrations of peptides were then added to induce lipid mixing between liposomes. Lipid mixing between labeled and unlabeled liposomes results in a dilution of fluorescent probes and an increase in dye fluorescence due to a relief of self-quenching. Fluorescence changes induced by peptides were recorded under constant stirring using a PC1 photon-counting spectrometer (ISS, USA) with $\lambda ex = 480$ nm and $\lambda em = 505$ nm. At the end of each recording, complete dequenching of the dye was induced by adding Triton X-100 (0.1% v/v final concentration). All experiments were performed at 37 °C. The degree of dye quenching was calculated as $Q(t) = 100 \times (F(t) - F0)/(Ftriton - F0)$, where $F(t)$, $F0$, and $Ftriton$ are fluorescence at time t, before the addition of peptide and after addition of Triton X-100, respectively. The initial rate (v0) and final extent (A0) of lipid mixing were estimated from the fit of the Q(t) curve by the expression $Q(t) = A0 - A0* \exp(-t/\tau)$ with $v0 = A0/\tau$.

PLIN1 AH peptide competition assay

PLIN1 AH peptides (human PLIN1 108-143: PPEKIA-SELKDTISTRLRSARNSISVPIASTSDKVL, FITC-modified or unmodified) were synthesized by ThermoFisher and dissolved in the emulsion buffer (20 mM Tris-HCl, 150 mM NaCl, pH 8.0) at a concentration of 1 mg/mL. Phospholipid (L-a-Phosphatidylcholine soybean, P7443, Sigma) was dissolved in chloroform at a concentration of 32 mM as a stock solution. A 5 µL aliquot of the phospholipid stock solution was dried under nitrogen stream in a 1.5 mL microcentrifuge tube, followed by the addition of 90 µL emulsion buffer, 5 µL Triolein (>99% purify, T7140 Sigma), and 5 µL PLIN1-AH-FITC. For neat oil droplets, 90 µL emulsion buffer was mixed with 5 µL triolein and 5 µL PLIN1-AH-FITC in a clean 1.5 ml microcentrifuge tube. The tubes were then vortexed manually at a fixed angle of ~30˚ for 10 cycles of 30 s on/30 s off at 25˚C and sonicated in a Bioruptor® Pico sonication device (B01080010) for 30 s at a medium frequency level to allow emulsion to happen. To start the competition assay, the emulsified neat oil droplets/phospholipid-coated droplets were mixed with an equal volume of unlabeled PLIN1 AH peptide solution to achieve a 20-fold excess of unlabeled PLIN1 AH peptide over FITC-labeled peptide. Droplet images were then captured at indicated time points with a Zeiss LSM900 confocal system and analyzed with ImageJ.

PLIN1-mCherry FRAP

Isolated primary brown adipocytes from BAT were cultured for two days and infected with a PLIN1-mCherry adenovirus for 24 h. Regions of interest were selected to ensure that one entire LD was included to avoid rapid recovery due to intra-LD exchange and then bleached by 100% laser power (546 diode laser), followed by time-lapse scanning with a 5-minute interval for a total 120 min. Fluorescence intensity of

PLIN1-mcherry on LD surface was quantitated by ImageJ and calculated as the percentage of the pre-bleach value.

Cycloheximide chase assay

Isolated stromal vascular fraction (SVF) from the BAT of 6–8 week old WT or *clstn3b*⁻/⁻ mice were seeded into 6-well plates and induced to differentiate following a previously published procedure (DMEM + 10% FBS + 1x penicillin/streptomycin and supplemented with 20 nM insulin, 1 mM dexamethasone, 0.5 mM isobutylmethylxanthine, 1 nM rosiglitazone, and 1 nM 3,3,5-triiodo-L thyronine for 2 days). Cells were then kept in a maintenance medium (DMEM + 10% FBS + 1x penicillin/streptomycin supplemented with 20 nM insulin and 1 nM rosiglitazone). On Day 6 post induction, cells were treated 100 µg/mL cycloheximide or vehicle in the maintenance medium for indicated time periods and protein was extracted for immunoblotting.

Real-time qPCR analysis

The following primers were used for qPCR analysis of gene expression. *Cd36*-fwd, GGACATTGAGATTCTTTTCCTCTG, rev, GCAAAGGCATTGGCTGGAAGAAC; *clstn3b*-fwd, CTCCGCAGGAACAGCAGCCC, rev, AGGATAACCATAAGCACCAG; *tnf*-fwd, GGTGCCTATGTCTCAGCCTCTT, rev, GCCATAGAACTGATGAGAGGGAG; *ccl2*-fwd, GCTACAAGAGGATCACCAGCAG, rev, GTCTGGACCCATTCCTTCTTGG; *adgre1*-fwd, CGTGTTGTTGGTGGCACTGTGA, rev, CCACATCAGTGTTCCAGGAGAC; *lipe*-fwd, TTGGGGAGCTCCAGTCGGA, rev, TCGTGCGTAAATCCATGCTGT; *fabp4*-fwd, ACACCGAGATTTCCTTCAAACTG, rev, CCATCTAGGGTTATGATGCTCTTCA; *L19*-fwd, GGTCTGGTTGGATCCCAATG, rev, CCCATCCTTGATCAGCTTCCT; *lpl*-fwd, GGGAGTTTGGCTCCAGAGTTT, rev, TGTGTCTTCAGGGGTCCTTAG; *cfd*-fwd, CATGCTCGGCCCTACATGG, rev, CACAGAGTCGTCATCCGTCAC; *cidec*-fwd, TCGGAAGGTTCGCAAAGGCATC, rev, CTCCACGATTGTGCCATCTTCC; *bscl2*-fwd, GTCTGTGTTCCTCTATGGCTCC, rev, CCAGTGAGACATTGGCAACAGG; *abhd5*-fwd, AGATGTGCCCTCAGGTTGGACA, rev, ATCTGGTCGCTCAGGAAAACCC; *plin1*-fwd, TACCTAGCTGCTTTCTCGGTG, rev, GTGGGCTTCTTTGGTGCTGT; *cidea*-fwd, ATCACAACTGGCCTGGTTACG, rev, TACTACCCGGTGTCCATTTCT.

Statistics and reproducibility

All data shown are mean ± s.e.m. Statistical significance was calculated by unpaired Student's two-sided *t*-test for comparisons between two groups and one-way ANOVA with Tukey's post hoc test for comparisons between three groups. Two-side Wilcoxon test was used for nonparametric test between samples deviating from normal distribution. Two-way Repeated Measurement ANOVA was used to analyze time-series data. All experiments have been successfully repeated with similar results at least three times.

Reporting summary

Further information on research design is available in the Nature Portfolio Reporting Summary linked to this article.

Data availability

The authors declare that all data supporting the findings of this study are available within the paper and its Supplementary Information files. Source data for all figures are provided with the paper. Processed results for the LD proteomics are provided in the Supplementary Information. Raw data have been deposited to MassIVE under accession number: MSV000095763 (https://massive.ucsd.edu/ProteoSAFe/dataset.jsp?task=fcce2845ab1647f883d90e521c9e75b4). Correspondence and requests for materials should be addressed to X.Z. Source data are provided with this paper.

References

1. Shulman, G. I. Ectopic fat in insulin resistance, dyslipidemia, and cardiometabolic disease. *N. Engl. J. Med.* **371**, 1131–1141 (2014).

2. Akazawa, S., Sun, F., Ito, M., Kawasaki, E. & Eguchi, K. Efficacy of troglitazone on body fat distribution in type 2 diabetes. *Diab. Care* **23**, 1067–1071 (2000).

3. Yki-Järvinen, H. Thiazolidinediones. *N. Engl. J. Med.* **351**, 1106–1118 (2004).

4. Lipscombe, L. L. et al. Thiazolidinediones and cardiovascular outcomes in older patients with diabetes. *JAMA* **298**, 2634–2643 (2007).

5. Greenberg, A. S. et al. The role of lipid droplets in metabolic disease in rodents and humans. *J. Clin. Invest.* **121**, 2102–2110 (2011).

6. Olzmann, J. A. & Carvalho, P. Dynamics and functions of lipid droplets. *Nat. Rev. Mol. Cell Biol.* **20**, 137–155 (2019).

7. Yan, R. et al. Human SEIPIN binds anionic phospholipids. *Dev. Cell* **47**, 248–256.e244 (2018).

8. Arlt, H. et al. Seipin forms a flexible cage at lipid droplet formation sites. *Nat. Struct. Mol. Biol.* **29**, 194–202 (2022).

9. Sui, X. et al. Cryo–electron microscopy structure of the lipid droplet–formation protein seipin. *J. Cell Biol.* **217**, jcb.201809067 (2018).

10. Krahmer, N. et al. Phosphatidylcholine synthesis for lipid droplet expansion is mediated by localized activation of CTP:phosphocholine cytidylyltransferase. *Cell Metab.* **14**, 504–515 (2011).

11. Kory, N., Farese, R. V. & Walther, T. C. Targeting fat: mechanisms of protein localization to lipid droplets. *Trends Cell Biol.* **26**, 535–546 (2016).

12. Dhiman, R., Caesar, S., Thiam, A. R. & Schrul, B. Mechanisms of protein targeting to lipid droplets: a unified cell biological and biophysical perspective. *Semin. Cell Dev. Biol.* **108**, 4–13 (2020).

13. Magré, J. et al. Identification of the gene altered in Berardinelli–Seip congenital lipodystrophy on chromosome 11q13. *Nat. Genet.* **28**, 365–370 (2001).

14. Gandotra, S. et al. Perilipin deficiency and autosomal dominant partial lipodystrophy. *N. Engl. J. Med.* **364**, 740–748 (2011).

15. Kozusko, K. et al. Clinical and molecular characterization of a novel PLIN1 frameshift mutation identified in patients with familial partial lipodystrophy. *Diabetes* **64**, 299–310 (2014).

16. Phillips, M. J. & Voeltz, G. K. Structure and function of ER membrane contact sites with other organelles. *Nat. Rev. Mol. Cell Biol.* **17**, 69–82 (2016).

17. Datta, S., Liu, Y., Hariri, H., Bowerman, J. & Henne, W. M. Cerebellar ataxia disease–associated Snx14 promotes lipid droplet growth at ER–droplet contactsSnx14 regulates ER–droplet contacts. *J. Cell Biol.* **218**, 1335–1351 (2019).

18. Du, X. et al. ORP5 localizes to ER–lipid droplet contacts and regulates the level of PI(4)P on lipid droplets. *J. Cell Biol.* **219**, e201905162 (2019).

19. Kumar, N. et al. VPS13A and VPS13C are lipid transport proteins differentially localized at ER contact sites. *J. Cell Biol.* **217**, 3625–3639 (2018).

20. Wang, H. et al. Seipin is required for converting nascent to mature lipid droplets. *eLife* **5**, e16582 (2016).

21. Xu, D. et al. Rab18 promotes lipid droplet (LD) growth by tethering the ER to LDs through SNARE and NRZ interactions. *J. Cell Biol.* **217**, 975–995 (2018).

22. Li, D. et al. The ER-localized protein DFCP1 modulates ER-lipid droplet contact formation. *Cell Rep.* **27**, 343–358.e345 (2019).

23. Freyre, C. A. C., Rauher, P. C., Ejsing, C. S. & Klemm, R. W. MIGA2 links mitochondria, the ER, and lipid droplets and promotes de novo lipogenesis in adipocytes. *Mol. Cell* https://doi.org/10.1016/j.molcel.2019.09.011 (2019).

24. Markgraf, D. F. et al. An ER protein functionally couples neutral lipid metabolism on lipid droplets to membrane lipid synthesis in the ER. *Cell Rep.* **6**, 44–55 (2014).

25. Song, J. et al. Identification of two pathways mediating protein targeting from ER to lipid droplets. *Nat. Cell Biol.* **24**, 1364–1377 (2022).

26. Zeng, X. et al. Innervation of thermogenic adipose tissue via a cal-syntenin 3β–S100b axis. *Nature* **569**, 229–235 (2019).

27. Qian, K. et al. CLSTN3β enforces adipocyte multilocularity to facilitate lipid utilization. *Nature* **613**, 160–168 (2023).

28. Chi, J. et al. Three-dimensional adipose tissue imaging reveals regional variation in beige fat biogenesis and PRDM16-dependent sympathetic neurite density. *Cell Metab.* **27**, 226–236.e223 (2018).

29. Tansey, J. T. et al. Perilipin ablation results in a lean mouse with aberrant adipocyte lipolysis, enhanced leptin production, and resistance to diet-induced obesity. *Proc. Natl Acad. Sci. USA* **98**, 6494–6499 (2001).

30. Wei, S. et al. Spontaneous development of hepatosteatosis in perilipin-1 null mice with adipose tissue dysfunction. *Biochim. Biophys. Acta Mol. Cell Biol. Lipids* **1863**, 212–218 (2018).

31. Chorlay, A. & Thiam, A. R. Neutral lipids regulate amphipathic helix affinity for model lipid droplets. *J. Cell Biol.* **219**, e201907099 (2020).

32. Meyers, N. L., Wang, L. & Small, D. M. Apolipoprotein C-I binds more strongly to phospholipid/triolein/water than triolein/water interfaces: a possible model for inhibiting cholesterol ester transfer protein activity and triacylglycerol-rich lipoprotein uptake. *Biochemistry* **51**, 1238–1248 (2012).

33. Ajjaji, D. et al. Dual binding motifs underpin the hierarchical association of perilipins1–3 with lipid droplets. *Mol. Biol. Cell* **30**, 703–716 (2019).

34. Abreu-Vieira, G. et al. Cidea improves the metabolic profile through expansion of adipose tissue. *Nat. Commun.* **6**, 7433 (2015).

35. Wu, L. et al. Cidea controls lipid droplet fusion and lipid storage in brown and white adipose tissue. *Sci. China Life Sci.* **57**, 107–116 (2014).

36. Gupta, A. et al. Human CIDEC transgene improves lipid metabolism and protects against high-fat diet-induced glucose intolerance in mice. *J. Biol. Chem.* **298**, 102347 (2022).

37. Lahiri, S. et al. A conserved endoplasmic reticulum membrane protein complex (EMC) facilitates phospholipid transfer from the ER to mitochondria. *PLoS Biol.* **12**, e1001969 (2014).

38. Raychaudhuri, S. & Prinz, W. A. Nonvesicular phospholipid transfer between peroxisomes and the endoplasmic reticulum. *Proc. Natl Acad. Sci. USA* **105**, 15785–15790 (2008).

39. Lees, J. A. & Reinisch, K. M. Inter-organelle lipid transfer: a channel model for Vps13 and chorein-N motif proteins. *Curr. Opin. Cell Biol.* **65**, 66–71 (2020).

40. Rothbard, J. B., Jessop, T. C., Lewis, R. S., Murray, B. A. & Wender, P. A. Role of membrane potential and hydrogen bonding in the mechanism of translocation of guanidinium-rich peptides into cells. *J. Am. Chem. Soc.* **126**, 9506–9507 (2004).

41. Allolio, C. et al. Arginine-rich cell-penetrating peptides induce membrane multilamellarity and subsequently enter via formation of a fusion pore. *Proc. Natl Acad. Sci. USA* **115**, 11923–11928 (2018).

42. Yang, S.-T., Zaitseva, E., Chernomordik, L. V. & Melikov, K. Cell-penetrating peptide induces leaky fusion of liposomes containing late endosome-specific anionic lipid. *Biophys. J.* **99**, 2525–2533 (2010).

43. Robison, A. D. et al. Polyarginine interacts more strongly and cooperatively than polylysine with phospholipid bilayers. *J. Phys. Chem. B* **120**, 9287–9296 (2016).

44. Andreev, K. et al. Guanidino groups greatly enhance the action of antimicrobial peptidomimetics against bacterial cytoplasmic membranes. *Biochim. Biophys. Acta Biomembr.* **1838**, 2492–2502 (2014).

45. Golani, G. et al. Myomerger promotes fusion pore by elastic coupling between proximal membrane leaflets and hemifusion diaphragm. *Nat. Commun.* **12**, 495 (2021).

46. Zhukovsky, M. A., Filograna, A., Luini, A., Corda, D. & Valente, C. Phosphatidic acid in membrane rearrangements. *FEBS Lett.* **593**, 2428–2451 (2019).

47. Chernomordik, L. V. & Kozlov, M. M. Membrane hemifusion: crossing a chasm in two leaps. *Cell* **123**, 375–382 (2005).

48. Paar, M. et al. Remodeling of lipid droplets during lipolysis and growth in adipocytes*. *J. Biol. Chem.* **287**, 11164–11173 (2012).

49. Lee, M. J., Puri, V. & Fried, S. K. Metabolic and structural remodeling during browning of primary human adipocytes derived from omental and subcutaneous depots. *Obesity* **32**, 70–79 (2024).

50. Bai, N. et al. Transcript profile of CLSTN3B gene in human white adipose tissue is associated with obesity and mitochondrial gene program. *Life Metab.* **2**, load037 (2023).

51. Chan, S. C., Lin, S.-C. & Li, P. Regulation of Cidea protein stability by the ubiquitin-mediated proteasomal degradation pathway. *Biochem. J.* **408**, 259–266 (2007).

52. Liu, L. et al. Deletion of cavin/PTRF causes global loss of caveolae, dyslipidemia, and glucose intolerance. *Cell Metab.* **8**, 310–317 (2008).

53. Razani, B. et al. Caveolin-1-deficient mice are lean, resistant to diet-induced obesity, and show hypertriglyceridemia with adipocyte abnormalities. *J. Biol. Chem.* **277**, 8635–8647 (2002).

Acknowledgements

Author contributions

X.Z. conceived the project. X.Z. and C.Z. designed the experiments. C.Z., D.Y., M.L., and X.Z. performed the experiments. K.M. performed the lipid mixing assay. M.Y. performed image and statistical analyses. G.V., K.E., and J.M. performed the lipidomics analysis. X.Z. and C.Z. wrote the manuscript. All authors participated in reviewing and discussing the manuscript.

Competing interests

The authors declare no competing interests.

Additional information

Supplementary information The online version contains supplementary material available at https://doi.org/10.1038/s41467-024-53750-z.

Correspondence and requests for materials should be addressed to Xing Zeng.

Peer review information *Nature Communications* thanks Vishwajeet Puri, Siegfried Ussar and the other anonymous reviewer(s) for their contribution to the peer review of this work. A peer review file is available.

Reprints and permissions information is available at http://www.nature.com/reprints

Publisher's note Springer Nature remains neutral with regard to jurisdictional claims in published maps and institutional affiliations.